

See discussions, stats, and author profiles for this publication at: <https://www.researchgate.net/publication/200730248>

# Modeling Dielectric Relaxation in Polymer Glass Simulations: Dynamics in the Bulk and in Supported Polymer Films

ARTICLE *in* MACROMOLECULES · OCTOBER 2008

Impact Factor: 5.8 · DOI: 10.1021/ma800694v

---

CITATIONS

45

---

READS

43

5 AUTHORS, INCLUDING:



Simone Peter

12 PUBLICATIONS 231 CITATIONS

SEE PROFILE



Simone Napolitano

Université Libre de Bruxelles

45 PUBLICATIONS 1,000 CITATIONS

SEE PROFILE



Michael Wübbenhorst

University of Leuven

163 PUBLICATIONS 2,606 CITATIONS

SEE PROFILE

# Modeling Dielectric Relaxation in Polymer Glass Simulations: Dynamics in the Bulk and in Supported Polymer Films

S. Peter,<sup>†</sup> S. Napolitano,<sup>‡</sup> H. Meyer,<sup>†</sup> M. Wübbenhorst,<sup>‡</sup> and J. Baschnagel<sup>\*†</sup>

*Institut Charles Sadron, CNRS UPR 22, Université Strasbourg 1, 23 rue du Loess-BP 84047, 67034 Strasbourg Cedex 2, France, and Laboratory of Acoustics and Thermal Physics, Department of Physics and Astronomy, Katholieke Universiteit Leuven, Celestijnenlaan 200D, B-3001 Leuven, Belgium*

*Received March 28, 2008; Revised Manuscript Received June 16, 2008*

**ABSTRACT:** We perform molecular dynamics simulations to study the dielectric relaxation of a bead–spring model for a polymer melt in the bulk and in supported films. By assigning dipole moments parallel and perpendicular to the backbone of all chains in the completed simulation trajectories, we calculate the dielectric spectra of so-called type-A polymers which exhibit relaxation processes due to the local motion of chain segments (“segmental mode”) and due to fluctuations of the end-to-end vector (“normal mode”). We investigate the dependence of both processes on film thickness and chain length and for the segmental mode also on temperature  $T$ . We find that the relaxation of both modes is enhanced in the films relative to the bulk. For the segmental mode this difference between film and bulk dynamics increases on cooling toward the glass transition. By a layer-resolved analysis of the segmental relaxation, we show that the acceleration of the average film dynamics is a consequence of a smooth gradient in relaxation, originating from both interfaces where the segmental dipoles relax much faster than in the bulk. Additionally, near the interfaces the segmental relaxation is more strongly stretched than in the center of the film where bulk behavior prevails. As the average film dynamics comprises contributions from all layers, the dielectric spectra of the films are broader than in the bulk at the same  $T$ . Finally, starting from the layer-resolved analysis which associates a dielectric function and so a capacitance with each layer, we suggest to think of a film as being a system of capacitors. The capacitors are arranged in series, if the electric ( $E$ ) field is perpendicular to the plane of the film (the usual experimental situation), and in parallel, if the field is parallel to the plane. Because of these different arrangements of the capacitors, the resulting dielectric spectra depend on the direction of the  $E$ -field. For instance, we find that, although the segmental relaxation in each layer is taken to be the same for both field directions, the average dielectric spectra differ because the layer-dependent dielectric strength and the limiting high-frequency permittivity ( $\epsilon_\infty$ ) enter into the average dielectric response in different ways for the  $E$ -field being perpendicular or parallel to the film plane.

## 1. Introduction

An appealing approach to evidencing the existence of a correlation length  $\xi_g$ , possibly associated with the vitrification process, should be the study of the glass transition in confined geometry. As  $\xi_g$  is expected to increase on cooling toward the glass transition temperature ( $T_g$ ), the finite dimension of the confinement should truncate this increase, entailing faster dynamics relative to the bulk at low temperature and thus a decrease of  $T_g$ .<sup>1</sup>

This perspective has been a major motivation for recent research on the glass transition of confined liquids and thin polymer films. The progress achieved in this field is described in several comprehensive reviews.<sup>2–7</sup> Indeed, many studies report deviations from bulk behavior if the glass former is confined to nanoscopic dimensions. However, unambiguous evidence for the existence of  $\xi_g$  is difficult to obtain due to the impact of nonuniversal interfacial effects.<sup>7–9</sup> Such effects may result from specific particle–substrate interactions, confinement-induced changes of the liquid structure or polymer conformations, density variations, and so on.

The glass transition of polymer films provides an example where interfacial effects can be prominent. For thin films supported on a substrate, many studies,<sup>10–30</sup> albeit not all<sup>31,32</sup> (see ref 33 for a possible explanation of this difference), find reductions in  $T_g$  with decreasing film thickness ( $h$ ) if the polymer–substrate interactions are not strongly attractive. This is the case e.g. for *i*-poly(methyl methacrylate) (*i*-PMMA) on

aluminum<sup>14,34</sup> or polystyrene (PS) on a variety of substrates.<sup>10,12,15,17–19,21–24,26–30</sup> For PS there is increasing evidence, e.g. from surface relaxation after nanodeformations<sup>35</sup> or direct measurement of the positional dependence of  $T_g$ ,<sup>26</sup> that the observed depression of  $T_g$  is caused by a “free-surface effect”. Monomers at and near the free surface have local environments differing from those in the bulk. It is natural to assume—and there is evidence from simulations<sup>36–41</sup>—that these monomers are more mobile than those in the center of the film, and this enhanced mobility should lead to reductions in  $T_g$  (see however ref 42 for a different point of view).

Several studies show that the strength of this free-surface effect depends on the monomer structure of the polymer<sup>20,27</sup> and on the substrate.<sup>11,25,30</sup> For instance, for PS small modifications of the repeat unit have a strong impact on the  $T_g$  reductions.<sup>27</sup> For PMMA on Si substrates, the sign of  $T_g$  shift depends on tacticity; with decreasing film thickness  $T_g$  increases for *i*-PMMA but decreases for *s*-PMMA.<sup>20</sup> Furthermore, for systems where the substrate strongly attracts the polymer, such as poly(2-vinylpyridine) (P2VP) on silica<sup>43,44</sup> or between aluminum layers,<sup>45</sup> the effect of the free surface can become annihilated by the substrate attraction. In this case, a strong increase of  $T_g$  is found for thin films, and it is even possible to remove the free surface by capping the P2VP film without affecting the shift of  $T_g$ .<sup>44</sup> Apparently, surface and substrate effects may strongly compete with each other in supported films. An attractive way to avoid this interplay seems to be the study of freely standing films. But even in this case differences are found. While PS films show very pronounced reductions of  $T_g$  with decreasing  $h$ ,<sup>12,46</sup> the depression is much weaker for

\* Corresponding author. E-mail: baschnag@ics.u-strasbg.fr.

<sup>†</sup> Université Strasbourg 1.

<sup>‡</sup> Katholieke Universiteit Leuven.

PMMA<sup>47,48</sup> and apparently absent for poly(vinyl acetate) (PVAc)<sup>49</sup> (at least for thicknesses down to about 30 nm<sup>49,50</sup>).

Most of the above studies measure (the average)  $T_g$ . As such, they provide information on the dynamic response of the system only on the time scale associated with  $T_g$  (which depends on the experimental conditions, such as the cooling rate<sup>33</sup>). However, the full relaxation behavior of polymers in nanoconfinement has also been studied by several techniques,<sup>5,6</sup> in particular by dielectric spectroscopy (DS).<sup>3,14,16,21,22,28–30,45,50–60</sup> By DS it is possible to simultaneously measure  $T_g$  and the relaxation spectrum, even for samples in thin film geometry. These techniques were applied to thin films of PS,<sup>21,22,28–30</sup> PMMA,<sup>14,16,51</sup> PVAc,<sup>50</sup> poly(ethylene terephthalate) (PET),<sup>58</sup> and *cis*-1,4-polyisoprene (*cis*-1,4 PI),<sup>52–56</sup> among others. An important feature emerging from these DS studies is that the  $\alpha$  process, i.e. the segmental relaxation associated with the glass transition, is broadened relative to the bulk, in particular for thin films. This broadening may result from a spatial heterogeneity of the dynamics in nanoconfinement. At the interfaces the segmental dynamics can be enhanced (e.g., at the free surface) or slowed down (e.g., at an attractive substrate) relative to the bulk. Chain segments in layers adjoining these interfacial layers should also have their dynamics perturbed, albeit to a lesser extent, which will lead to a still weaker perturbation for the next layer, and so on. This interpretation corresponds to a smooth transition from interface-induced perturbations of the relaxation to bulk dynamics with increasing distance from the interfaces. This idea has recently been used to interpret dielectric spectra of nanostructured diblock copolymer melts<sup>60</sup> and is consistent with the positional dependence of  $T_g$  found in multilayer films of labeled and unlabeled PS.<sup>26</sup>

Results from computer simulations of confined glass-formers also support this view of an interface-induced gradient in relaxation (see ref 61 for a review). Many simulations study the relaxation behavior and  $T_g$  in thin films of simple binary liquids<sup>62,63</sup> or polymer melts (often bead–spring models).<sup>37–41,64–66</sup> They show that the relaxation behavior is fairly complex and results from the following effects:<sup>39,61,63</sup> (i) the bulklike slowing down of the dynamics on cooling toward  $T_g$ ; (ii) a smooth transition of enhanced or retarded relaxation relative to the bulk from the interfaces to the interior of the confined liquid; (iii) a growing range of this transition on cooling so that interface-induced perturbations of the dynamics may propagate across the entire liquid for sufficiently strong confinement and/or low temperature. These effects are responsible for shifts of  $T_g$  in the simulation, similar to those described above for experiments.

Many of the above simulations explore the structural relaxation by dynamic correlation functions, such as the incoherent scattering function or mean-square displacements. To our knowledge, no simulation work on dielectric relaxation has been performed. With the present paper we want to extend our recent studies<sup>39,50</sup> in this direction. Section 2 briefly introduced the simulation model—a bead–spring model for a polymer melt—and describes how we attach electric dipole moments to the chains. With this model we calculate the correlation function of the polarization and via the fluctuation–dissipation theorem the complex dielectric function. Results in time and frequency domain for both the bulk dynamics and the average film dynamics are presented in sections 3 and 4. This discussion is complemented by a layer-resolved analysis of the film dynamics (section 5). Inspired by this layer-resolved analysis, we propose in section 6 a modeling of experimental film spectra by a system of capacitors. The final section 7 presents our conclusions.

## 2. Computational Details and Analyzed Quantities

**2.1. Model and Simulation.** We examine a bead–spring model<sup>39</sup> for a polymer melt. In this model nonbonded monomers interact by a truncated and shifted Lennard-Jones (LJ) potential

$$U_{\text{LJ}}(r) = 4\epsilon \left[ \left( \frac{\sigma}{r} \right)^{12} - \left( \frac{\sigma}{r} \right)^6 \right] - U_{\text{LJ}}(r_c), \quad r \leq r_c \quad (1)$$

where the cutoff distance is given by  $r_c = 2.3\sigma \approx 2r_{\text{min}}$  ( $r_{\text{min}}$  is the minimum of the LJ potential). For nearest neighbors along the chain the LJ interaction is not included. These monomers are connected by a harmonic bond potential

$$U_{\text{bond}}(r) = \frac{k}{2}(r - r_0)^2 \quad (2)$$

with equilibrium bond length  $r_0 = 0.967\sigma$  and spring constant  $k = 1111\epsilon/\sigma^2$ . In the following, all data will be presented in LJ units, that is,  $\epsilon = 1$ ,  $\sigma = 1$ , and mass  $m = 1$ . This means that temperature  $T$  is measured in units of  $\epsilon/k_B$  (Boltzmann constant  $k_B = 1$ ) and time  $t$  in units of  $(m\sigma^2/\epsilon)^{1/2}$ .

The large value for  $k$  in eq 2 prevents the chains from crossing each other in the course of the simulation so that entanglements can form. The entanglement length of our model is  $N_e = 32$ .<sup>67,68</sup> In the following, we mainly discuss data for nonentangled and slightly entangled chains of length  $N = 10$  and 64, respectively. However, results at high  $T$  for a longer chain,  $N = 256$ , will also be shown.

For these chain lengths we study bulk polymer melts and supported polymer films by molecular dynamics (MD) simulations under isobaric and isothermal (DPD thermostat<sup>69</sup>) conditions. The supported films have a polymer–wall and a polymer–vacuum interface. (For  $N = 10$  and 64 bulk and film systems comprise 3072 monomers, whereas the systems for  $N = 256$  contain 12 288 monomers.) Since no external force acts on the monomers at the polymer–vacuum interface, the pressure  $p$  vanishes. The MD simulations are therefore carried out at  $p = 0$ . We integrate the equations of motion by the velocity Verlet algorithm<sup>70</sup> with a step size of  $\Delta t = 0.005$ . To equilibrate the initial configurations for  $N \geq 64$ , we combine the MD with double-bridging Monte Carlo (MC) moves.<sup>71,72</sup> Only few of these MC moves are accepted per unit time so that the stability and accuracy of the MD do not deteriorate. The MC moves, however, allow an efficient equilibration of large-scale conformational features.

For the simulation of supported films a wall must be introduced in the model. We place a completely smooth and laterally structureless wall at  $y = 0$  in the  $xz$ -plane of the simulation box by choosing for the monomer–wall interaction a (nontruncated) 9–3 LJ potential

$$U_{\text{wall}}(y) = \epsilon_w \left[ \left( \frac{1}{y} \right)^9 - \left( \frac{1}{y} \right)^3 \right] \quad (3)$$

Here  $y$  denotes the distance from the wall in perpendicular direction and  $\epsilon_w$  is the potential strength. We take  $\epsilon_w = 3$ , which is close to the wetting transition of the model.<sup>73</sup> Further details about the simulation procedure and the method employed to prepare the films may be found in ref 39.

Before leaving this section on the simulation model, we want to comment on an apparent qualitative difference between our and the experimental setup. We study supported polymer films with one free surface, whereas DS experiments are usually carried out on films that are confined between two electrodes. Typically, this sandwich geometry is created in an asymmetric fashion. First, thin films are prepared by spin-coating the polymer from solution onto an aluminum-coated capacitor plate, and then, after annealing a second electrode is evaporated on top of the free surface of the films. Although the films do thus not have a true free surface, DS experiments for PS,<sup>21,28,29,42</sup>

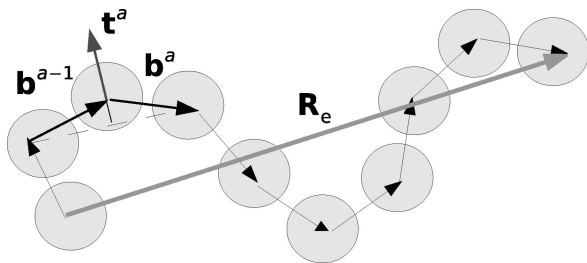


**Figure 1.** Illustration of the definition of the dipole moments for the monomers of a chain. The parallel dipole moment points in direction of the unit bond vector  $\mathbf{b}^a$ . These unit vectors add up to the vector  $\mathbf{R}$  which is proportional to the end-to-end vector  $\mathbf{R}_e$  of the chain (eq 8). The second dipole moment points in direction of  $\mathbf{t}^a$  which is defined by the difference of two consecutive bond vectors (eq 5). The vector  $\mathbf{t}^a$  is locally perpendicular to the chain, i.e., to the internal distance vector  $\mathbf{r}^{a+1} - \mathbf{r}^{a-1}$  (dashed line).

i-PMMA,<sup>14</sup> or *cis*-1,4 PI<sup>74</sup> suggest that free surface effects are not suppressed by the addition of the top electrode (see refs 30 and 75 for further discussion). A qualitative comparison between our simulation and DS results should thus be possible.

**2.2. Modeling the Polarization of Type A Polymers.** The term “type A polymers” refers to a class of linear polymers whose monomers carry an electric dipole moment which has a component parallel to the chain contour.<sup>74</sup> A well-studied example is *cis*-1,4-PI.<sup>55,74,77–81</sup> Because of the structure of the repeat unit, *cis*-1,4 PI has components of the dipole moment not only parallel but also perpendicular to the chain. The magnitude of these components is, however, small.<sup>77</sup> So it is plausible to assume that the dipole moments, albeit sufficient to provide a (weak) dielectric response, do not influence the structure and dynamics of PI significantly. This assumption was made in a chemically realistic simulation of *cis*-1,4-PI.<sup>81</sup> In this work, time series of melt configurations were created without including dipolar interactions in the force field, and a dipole moment was assigned a posteriori to each monomer of the completed simulation trajectories in order to study dielectric relaxation. The same approach was also taken in a chemically realistic simulation of polybutadiene<sup>82</sup> and by Barbieri et al.<sup>83</sup> in an MD study of local and large-scale motions of a bead–spring model for a polymer melt. For bead–spring models, defined by interaction potentials like those of eqs 1 and 2, the a posteriori introduction of dipole moments represents the only way to model dielectric relaxation. Therefore, we closely follow ref 83 in the present work.

We define two local dipole moments: one parallel to the chain backbone and the other perpendicular to it (Figure 1). The parallel dipole has the magnitude  $\mu_N$  and is oriented along the normalized bond vector

$$\mathbf{b}_j^a = \frac{\mathbf{r}_j^{a+1} - \mathbf{r}_j^a}{|\mathbf{r}_j^{a+1} - \mathbf{r}_j^a|} \approx \frac{1}{r_0}(\mathbf{r}_j^{a+1} - \mathbf{r}_j^a) \quad (4)$$

Here  $\mathbf{r}_j^a$  denotes the position of monomer  $a$  ( $= 1, \dots, N$ ) on chain  $j$  ( $= 1, \dots, n$ ). The last approximate equality holds because the bond length  $|\mathbf{r}_j^{a+1} - \mathbf{r}_j^a|$  is constrained to be close to the equilibrium value  $r_0$  by the stiff bond potential, eq 2. The perpendicular dipole has the magnitude  $\mu_{\text{seg}}$  and points in the direction of

$$\mathbf{t}_j^a = (-1)^a(\mathbf{b}_j^a - \mathbf{b}_j^{a-1}) \quad (5)$$

The vector  $\mathbf{t}_j^a$  is locally perpendicular to the chain backbone, as demonstrated in ref 83. Following ref 83 we set  $\mu_{\text{seg}} = 1.5$  and  $\mu_N = 1$  because the ratio  $\mu_{\text{seg}}/\mu_N = 1.5$  corresponds to the one found for *cis*-1,4-PI.<sup>77</sup>

Utilizing these local dipole moments, we can introduce the dipole moment  $\mu_j(t)$  of chain  $j$  at time  $t$

$$\begin{aligned} \mu_j(t) &= [\mu_{\text{seg}} \mathbf{T}_j(t) + \mu_N \mathbf{R}_j(t)] \\ &= \mu_{\text{seg},j}(t) + \mu_{N,j}(t) \end{aligned} \quad (6)$$

Here  $\mathbf{T}_j(t)$  is the sum of the perpendicular dipoles over all monomers

$$\mathbf{T}_j(t) = \sum_{a=2}^{N-1} \mathbf{t}_j^a(t) \quad (7)$$

and  $\mathbf{R}_j(t)$  is proportional to the instantaneous end-to-end vector,  $\mathbf{R}_{e,j}(t)$ , of chain  $j$

$$\mathbf{R}_j(t) = \sum_{a=1}^{N-1} \mathbf{b}_j^a(t) \approx \frac{1}{r_0} \mathbf{R}_{e,j}(t) \quad (8)$$

The last approximate equality holds because  $|\mathbf{r}_j^{a+1}(t) - \mathbf{r}_j^a(t)| \approx r_0$  (see eq 4).

If we sum  $\mu_j(t)$  over all chains, we obtain the total dipole moment  $\mu^{\text{col}}(t)$  of the melt at time  $t$

$$\begin{aligned} \mu^{\text{col}}(t) &= \sum_{j=1}^n \mu_j(t) \\ &= \sum_{j=1}^n [\mu_{\text{seg},j}(t) + \mu_{N,j}(t)] \\ &= \mu_{\text{seg}}^{\text{col}}(t) + \mu_N^{\text{col}}(t) \end{aligned} \quad (9)$$

$\mu^{\text{col}}(t)$  is proportional to the polarization—i.e., the total dipole moment density—of the system. It is a collective quantity which decomposes, like  $\mu_j(t)$ , into two parts: a “segmental” part resulting from the perpendicular dipoles  $[\mu_{\text{seg}}^{\text{col}}(t)]$  and a “normal” part due to the parallel dipoles  $[\mu_N^{\text{col}}(t)]$ . We discuss these parts in the next section.

**2.3. Correlation Functions of the Polarization.** Dynamic properties can be investigated by the correlation function of the total dipole moment, i.e., by the polarization correlation function

$$C_{\text{tot}}^{\text{col}}(t) = \frac{\langle \mu^{\text{col}}(t) \cdot \mu^{\text{col}}(0) \rangle}{\langle \mu^{\text{col}}(0)^2 \rangle} \quad (10)$$

This collective correlation function is a sum of the many cross-correlations between the different dipole moments of the chains, such as  $\langle \mu_{\text{seg},j}(t) \cdot \mu_{N,k}(0) \rangle$ . Accounting for these cross-correlations in a theoretical analysis of experimental data is a formidable task. Therefore, the following assumptions are commonly made in the literature:<sup>78,81,83</sup>

1. Cross-correlations between different chains  $j$  and  $k$  are neglected. That is

$$\begin{aligned} \langle \mu^{\text{col}}(t) \cdot \mu^{\text{col}}(0) \rangle &= \sum_{j=1}^n \langle \mu_j(t) \cdot \mu_j(0) \rangle + \sum_{j \neq k} \langle \mu_j(t) \cdot \mu_k(0) \rangle \\ &\approx \sum_{j=1}^n \langle \mu_j(t) \cdot \mu_j(0) \rangle \equiv n \langle \mu(t) \cdot \mu(0) \rangle \end{aligned}$$

so that

$$C_{\text{tot}}^{\text{col}}(t) \approx C_{\text{tot}}(t) = \frac{\langle \mu(t) \cdot \mu(0) \rangle}{\langle \mu(0)^2 \rangle} \quad (11)$$

Thus, the collective correlation function of the melt,  $C_{\text{tot}}^{\text{col}}(t)$ , is replaced by the correlation function of the polarization of a single chain,  $C_{\text{tot}}(t)$ .

2. From eq 6 or 9 we expect that  $C_{\text{tot}}^{\text{col}}(t)$  or  $C_{\text{tot}}(t)$  reveals two distinct relaxation processes: a “segmental process” related to a reordering of the perpendicular dipole moments



$$\begin{aligned}
C_{\text{seg}}^{\text{col}}(t) &= \frac{\langle \mu_{\text{seg}}^{\text{col}}(t) \mu_{\text{seg}}^{\text{col}}(0) \rangle}{\langle |\mu_{\text{seg}}^{\text{col}}(0)|^2 \rangle} \\
&\simeq C_{\text{seg}}(t) \\
&= \frac{\langle \mu_{\text{seg}}(t) \mu_{\text{seg}}(0) \rangle}{\langle |\mu_{\text{seg}}(0)|^2 \rangle}
\end{aligned} \quad (12)$$

and a “normal-mode process” corresponding to the relaxation of the parallel polarization and thus to the reorientation of the end-to-end vector

$$\begin{aligned}
C_N^{\text{col}}(t) &= \frac{\langle \mu_N^{\text{col}}(t) \mu_N^{\text{col}}(0) \rangle}{\langle |\mu_N^{\text{col}}(0)|^2 \rangle} \\
&\simeq C_N(t) \\
&= \frac{\langle \mu_N(t) \mu_N(0) \rangle}{\langle |\mu_N(0)|^2 \rangle}
\end{aligned} \quad (13)$$

In the second line of eqs 12 and 13 we applied the previous assumption to neglect cross-correlations between different chains, and we introduced the single-chain quantities

$$\begin{aligned}
\langle \mu_{\text{seg}}(t) \mu_{\text{seg}}(0) \rangle &= \frac{\mu_{\text{seg}}^2}{n} \sum_{j=1}^n \langle \mathbf{T}_j(t) \cdot \mathbf{T}_j(0) \rangle \\
\langle \mu_N(t) \mu_N(0) \rangle &= \frac{\mu_N^2}{n} \sum_{j=1}^n \langle \mathbf{R}_j(t) \cdot \mathbf{R}_j(0) \rangle
\end{aligned} \quad (14)$$

For large  $N$  the relaxation times of the segmental and normal modes should be very different because the segmental mode probes local processes which depend only weakly, if at all, on  $N$ , whereas the normal mode strongly slows down with increasing  $N$ . Thus, in most experimental and numerical studies (see ref 83 and references therein) it is assumed that the segmental and normal modes decouple.  $C_{\text{tot}}(t)$  may then be approximated by

$$C_{\text{tot}}(t) \simeq C(t) \equiv w_{\text{seg}} C_{\text{seg}}(t) + w_N C_N(t) \quad (15)$$

where the weights  $w_{\text{seg}}$  and  $w_N$  are given by

$$\begin{aligned}
w_{\text{seg}} &= \frac{\mu_{\text{seg}}^2 \langle \mathbf{T}^2 \rangle}{\mu_N^2 \langle \mathbf{R}^2 \rangle + \mu_{\text{seg}}^2 \langle \mathbf{T}^2 \rangle} \\
w_N &= \frac{\mu_N^2 \langle \mathbf{R}^2 \rangle}{\mu_N^2 \langle \mathbf{R}^2 \rangle + \mu_{\text{seg}}^2 \langle \mathbf{T}^2 \rangle}
\end{aligned} \quad (16)$$

with

$$\begin{aligned}
\langle \mathbf{T}^2 \rangle &= \frac{1}{n} \sum_{j=1}^n \langle |\mathbf{T}_j(0)|^2 \rangle \\
\langle \mathbf{R}^2 \rangle &= \frac{1}{n} \sum_{j=1}^n \langle |\mathbf{R}_j(0)|^2 \rangle \simeq \frac{1}{r_0^2} R_c^2
\end{aligned} \quad (17)$$

and  $R_c^2$  being the mean-square end-to-end distance. We discuss the validity of assumptions 1 and 2 in the next section.

### 3. Results in the Time Domain

**3.1. Bulk Dynamics.** Figure 2a shows the relaxation of the segmental mode of a bulk melt ( $N = 64$ ) for temperatures close to the critical temperature  $T_c$  of mode-coupling theory (MCT),  $T_c^{N=64} = 0.415$ .<sup>40</sup> From these results two observations can be made. First, collective and single-chain correlation functions closely agree with each other. This supports the assumption  $C_{\text{seg}}^{\text{col}}(t) \simeq C_{\text{seg}}(t)$  of eq 12 and implies that, despite the dense, liquidlike packing of the monomers in the cold melt, interchain correlations of the perpendicular local dipole moments are very weak. If the chains decouple for the segmental process, we may

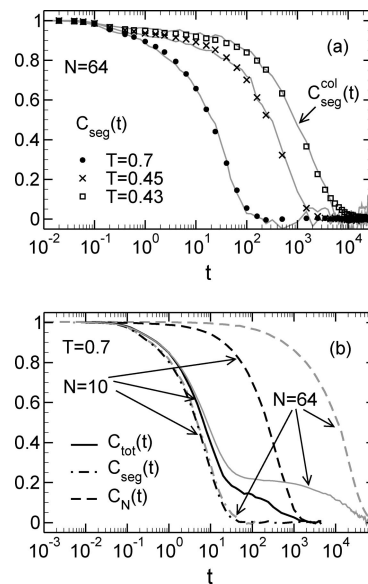


**Figure 2.** (a) Collective correlation function,  $C_{\text{seg}}^{\text{col}}(t)$  (lines), and single-chain correlation function,  $C_{\text{seg}}(t)$  (symbols), of the segmental mode in the bulk. All data refer to  $N = 64$  and temperatures above the critical temperature  $T_c$  of MCT. As we average over  $n$  measurements ( $n$  = number of chains), the numerical precision of  $C_{\text{seg}}(t)$  is much better than for  $C_{\text{seg}}^{\text{col}}(t)$ . (b) Total correlation function  $C_{\text{tot}}(t)$  (eq 11), segmental mode  $C_{\text{seg}}(t)$  (eq 12), and normal mode  $C_N(t)$  (eq 13) in the bulk for  $N = 10$  (black lines) and  $N = 64$  (gray lines) at  $T = 0.7$  ( $T_c^{N=10} = 0.405$ ;  $T_c^{N=64} = 0.415$ ).<sup>39,40</sup>

expect this decoupling to hold also for the normal mode because there should be no orientational correlations of the end-to-end vector in the polymer liquid. (A critical test of the latter assumption was not possible with the present data due to the lack of sufficient statistics.) Therefore, we focus on the single-chain quantities  $C_{\text{seg}}(t)$ ,  $C_N(t)$ , and  $C_{\text{tot}}(t)$  in the following.

The second observation concerns the time dependence of  $C_{\text{seg}}(t)$ . Figure 2a indicates that  $C_{\text{seg}}(t)$  relaxes in two steps at low  $T$ . The first step occurs around  $t \approx 0.2$  and represents the crossover from vibrational to relaxation dynamics. It leads to an intermediate time window where the relaxation is very protracted and  $C_{\text{seg}}(t)$  almost plateaus (“plateau regime”). In the second step,  $C_{\text{seg}}(t)$  leaves the plateau regime and decays to zero (“ $\alpha$ -relaxation”). The plateau regime increases in size with decreasing  $T$ , thus shifting the  $\alpha$ -relaxation to longer times.

We find similar two-step relaxations for all structural relaxation functions (coherent and incoherent scattering functions, mean-square displacements, Rouse modes, etc.) in the bulk<sup>39,61</sup> and in thin films<sup>39,40,61</sup> on cooling toward  $T_c$ . A two-step relaxation of dynamic correlation functions is a main prediction of the (ideal) MCT for  $T > T_c$  and is a consequence of the “caging” of the monomers by the nearest neighbors. Detailed comparisons<sup>61,84</sup> between MCT and our bulk simulations suggest that the relaxation mechanism proposed by MCT represents an important element to interpret the structural relaxation of our model. We thus employ ideas from MCT to explain qualitatively why the plateau of  $C_{\text{seg}}(t)$  is so high that the two-step relaxation is barely visible.

MCT provides an approximate theoretical framework to describe the slow relaxation of density fluctuations, such as  $\exp(i\mathbf{q} \cdot \mathbf{r}_f^q)$ , in the cold melt.  $C_{\text{seg}}(t)$ , on the other hand, can be expressed in terms of the correlation function of the monomer positions  $\mathbf{r}_f^q$ . A relation between both correlation functions can be established by observing that  $\exp(i\mathbf{q} \cdot \mathbf{r}_f^q) \simeq 1 + i\mathbf{q} \cdot \mathbf{r}_f^q$  in the limit  $q \rightarrow 0$ . Thus, the segmental mode is related to the small- $q$  limit of single-chain density fluctuations. In this limit, MCT predicts—and simulation finds—that the height of the plateau

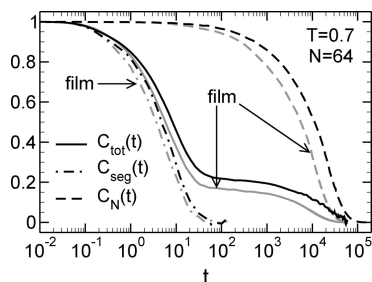


**Figure 3.** Various polarization correlation functions for a supported film of thickness  $h = 7.5 \approx 2R_g^{\text{bulk}}$  (gray lines) and for the bulk (black lines): total correlation function  $C_{\text{tot}}(t)$  (solid lines), segmental mode  $C_{\text{seg}}(t)$  (dash-dotted lines), and normal mode  $C_N(t)$  (dashed lines). All data refer to  $T = 0.7$  and  $N = 64$ .

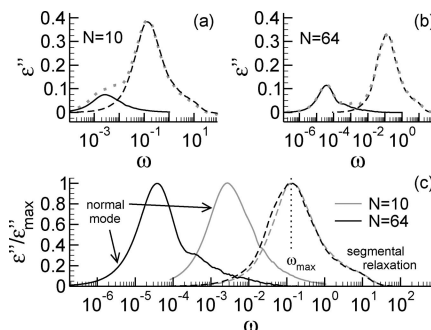
of the single-chain density fluctuations tends to 1.<sup>61,84</sup> Therefore, the plateau value of  $C_{\text{seg}}(t)$  should be high, making the first step of the two-step relaxation barely visible.

Figure 2b shows  $C_{\text{seg}}(t)$  for  $N = 10$  and 64 at  $T = 0.7$  and compares  $C_{\text{seg}}(t)$  to the normal mode  $C_N(t)$  and the total correlation function  $C_{\text{tot}}(t)$ . As expected, we find that the segmental relaxation is independent of chain length, whereas the normal mode strongly slows down with increasing  $N$ . This implies that  $C_{\text{tot}}(t)$  displays a two-step relaxation already at high  $T$ . This two-step relaxation is not due to monomer caging; the first step is related to  $C_{\text{seg}}(t)$  and the second to  $C_N(t)$ . Thus, the superposition approximation of eq 16,  $C_{\text{tot}}(t) \approx C(t)$ , should apply for large  $N$ . Equation 15 indeed holds for  $N = 64$ . For  $N = 10$ , however, small deviations between  $C_{\text{tot}}(t)$  and  $C(t)$  are found for intermediate times, in agreement with the results of ref 83. This demonstrates that for short chains there is some cross-correlation between the segmental and normal processes, but this correlation diminishes (rapidly) with increasing  $N$ .

**3.2. Average Film Dynamics.** Figure 3 illustrates the influence of geometric confinement on the relaxation of the polarization. For  $N = 64$  and  $T = 0.7$  the figure depicts  $C_{\text{seg}}(t)$ ,  $C_N(t)$ , and  $C_{\text{tot}}(t)$  obtained for the bulk and a supported film of thickness  $h = 7.5 \approx 2R_g^{\text{bulk}}$  where  $R_g^{\text{bulk}} (= 4.1)$  is the bulk radius of gyration.

For the segmental mode we see that bulk and film data are close to each other, although the relaxation in the film is systematically faster. This observation agrees with results obtained in previous work analyzing various mean-square displacements and the incoherent scattering function.<sup>39,40,61</sup> These studies suggested that the fast relaxation in our films is caused by the spatial heterogeneity of the film dynamics. Monomers at the free and supported interfaces move much further than they would in the bulk at the same temperature. These fast monomers make monomers in the neighboring layer also to move further than in the bulk, albeit to a lesser extent. These monomers in turn excite higher than bulk mobility in the next deeper layer and so on until the stimulus induced by the interfaces is damped and bulk dynamics is recovered in the film center. Thus, the fast relaxation of the interfacial layers continuously turns into bulklike relaxation with increasing distance from the interfaces.  $C_{\text{seg}}(t)$  in Figure 3 represents an average over all distances from the interfaces and as such aggregates contributions from the relaxation of interfacial and inner regions of the film. This explains why  $C_{\text{seg}}(t)$  decays in the films faster than in the bulk.

By the same token, we also expect the normal mode to have enhanced dynamics relative to the bulk. Figure 3 supports this expectation. Furthermore, the figure shows that the total correlation function  $C_{\text{tot}}(t)$  in the film lies systematically below the bulk  $C_{\text{tot}}(t)$ . Since  $C_{\text{tot}}(t)$  for  $N = 64$  is well approximated by the superposition of the segmental and normal modes (eq



**Figure 4.** Dielectric loss spectra for the segmental mode (dashed line), the normal mode (solid line), and the total correlation function  $C_{\text{tot}}(t)$  (dotted line). All data refer to the bulk at  $T = 0.7$ . (a) Results for  $N = 10$ . (b) Results for  $N = 64$ . (c)  $\epsilon''(\omega)/\epsilon''_{\text{max}}$  for the segmental and normal modes of  $N = 10$  (gray lines) and 64 (black lines).  $\epsilon''_{\text{max}}$  is the value of the dielectric loss at the peak position of the segmental and the normal mode. For the segmental mode the peak position  $\omega_{\text{max}}$  is indicated by a vertical dotted line.

15), an explanation for the latter finding is as follows: The film thickness,  $h = 7.5 \approx 2R_g^{\text{bulk}}$ , is comparable to the size of the unperturbed chain in the bulk. This implies that the perpendicular component of the end-to-end vector in the film,  $R_{e,y}$ , is depressed relative to its bulk value, whereas the in-plane components,  $R_{e,x}$  and  $R_{e,z}$ , are still bulklike (see e.g. ref 85). Therefore, the end-to-end distance of the film is smaller than in the bulk. On the other hand, we find that  $\langle r^2 \rangle$  (eq 7) is not modified relative to its bulk value. From eqs 16 and 17 we then see that  $w_{\text{seg}}$  is larger in the film than in the bulk, while  $w_N$  is smaller. Thus,  $C_{\text{tot}}(t)$  of the film lies below the bulk correlation function.

#### 4. Dielectric Loss Spectra: Bulk and Average Film Dynamics

Through the fluctuation–dissipation theorem (FDT)<sup>86</sup> it is possible to calculate the complex dielectric function  $\epsilon^*(\omega)$  by the Fourier transform of  $C_{\text{tot}}(t)$

$$\frac{\epsilon^*(\omega) - \epsilon_\infty}{\Delta\epsilon} = -F\left[\frac{\partial}{\partial t}C_{\text{tot}}(t)\right](\omega) = 1 - i\omega \int_0^\infty C_{\text{tot}}(t)e^{-i\omega t} dt \quad (18)$$

The dielectric function  $\epsilon^*(\omega) = \epsilon'(\omega) - i\epsilon''(\omega)$  consists of a real part  $\epsilon'(\omega)$  and an imaginary part  $\epsilon''(\omega)$ , the latter being referred to as dielectric loss (spectrum).<sup>87</sup> The (real) dielectric strength  $\Delta\epsilon = \epsilon_s - \epsilon_\infty$  is given by the difference of the limiting low-frequency,  $\epsilon_s = \epsilon'(0)$ , and high-frequency,  $\epsilon_\infty = \epsilon'(\infty)$ , value of  $\epsilon'(\omega)$ .

The Fourier transform in eq 18 is carried out by a trapezoidal Filon algorithm<sup>88</sup> on a logarithmic grid in both time and frequency domain. For slowly varying functions this calculation is more efficient than the application of a fast Fourier transform.

Figure 4 shows the dielectric loss spectra corresponding to the data discussed in Figure 2b, that is,  $\epsilon''(\omega)$  for  $C_{\text{tot}}(t)$ ,  $C_{\text{seg}}(t)$ , and  $C_N(t)$  of the bulk for  $N = 10$  and 64 at  $T = 0.7$ . The results support the main conclusions drawn before: (i) For  $N = 10$  the dielectric loss of segmental and normal modes overlap, whereas they are well separated for  $N = 64$  (Figure 4a,b). The superposition approximation of eq 15 thus holds for  $N = 64$ , whereas there are deviations at intermediate  $\omega$  for  $N = 10$ . (ii)  $\epsilon''(\omega)$  of the normal mode exhibits a strong dependence on chain length—it shifts to lower frequency with increasing  $N$ —while the loss spectrum of the segmental mode is affected by chain length only very weakly (Figure 4c).

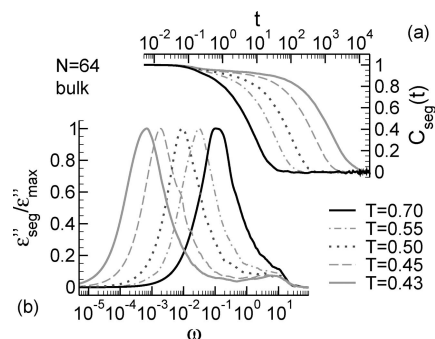


**Figure 5.** (a) Correlation function  $C_{\text{seg}}(t)$  of the segmental mode in the bulk for chains of length  $N = 64$  and various temperatures as indicated ( $T_c = 0.415$ ). (b) Dielectric loss spectra  $\epsilon''_{\text{seg}}(\omega)$  for the same system. The spectra are normalized by the maximum value  $\epsilon''_{\text{max}} = \epsilon''_{\text{seg}}(\omega_{\text{max}})$ .

#### 4.1. Temperature Dependence of the Segmental Mode.

Figure 5 illustrates the temperature dependence of the segmental mode for  $N = 64$ . As pointed out in the discussion of Figure 2a, the slowing down of the  $\alpha$ -relaxation on cooling is accompanied by the appearance of a plateau regime at intermediate times so that  $C_{\text{seg}}(t)$  relaxes in two steps (Figure 5a). The first step corresponds to the crossover from vibrational to relaxation dynamics and the second step to the  $\alpha$ -relaxation. The dielectric loss spectra should thus display two peaks that are separated by a minimum: Each peak corresponds to one step of the relaxation and the minimum to the center of the plateau regime. Figure 5b reveals that  $\epsilon''_{\text{seg}}(\omega)$  clearly exhibits only the low-frequency peak related to the  $\alpha$ -relaxation. The minimum and the first peak are barely visible. This is expected because the first relaxation step of  $C_{\text{seg}}(t)$  is not very pronounced due to the high value of the plateau (Figure 5a). (High plateau values are not uncommon to dielectric spectroscopy and are one of the reasons rendering an MCT analysis of the minimum of  $\epsilon''(\omega)$  difficult;<sup>89</sup> see also Chapters 4 and 5 of ref 87 for further detailed discussion.) Thus, we focus on the  $\alpha$ -process in the following.

The  $\alpha$ -process displays two features characteristic of all structural relaxation functions (scattering functions, mean-square displacements, Rouse modes, etc.) of our model (see ref 61 for a review): (i) For  $T > T_c$ , we find a time-temperature superposition property. That is, it is possible to superimpose  $C_{\text{seg}}(t)$  or  $\epsilon''(\omega)$  for different  $T$  onto a common master curve by scaling the time or frequency axis by the position  $\omega_{\text{max}}(T)$  of the  $\alpha$ -peak of  $\epsilon''(\omega)$ . (ii) On cooling  $\omega_{\text{max}}(T)$  decreases with  $T$  in a non-Arrhenius fashion.

The non-Arrhenius-like temperature dependence of the  $\alpha$ -time scale can be fitted either by the MCT prediction<sup>39,40,61</sup>

$$\omega_{\text{max}}(T) \propto (T - T_c)^{\gamma} \quad (19)$$

provided  $T$  is not too close to  $T_c$  (see e.g. ref 61 for a discussion of the applicability of eq 19), or by the Vogel–Fulcher–Tammann (VFT) equation

$$\omega_{\text{max}}(T) \propto \exp\left(-\frac{DT_0}{T - T_0}\right) \quad (20)$$

where  $T_0$  denotes the Vogel–Fulcher temperature and  $D$  is related to the fragility of the glass-former.<sup>1,90</sup>

Within the 2–3 decades in time accessible to our simulation, both the MCT and VFT formulas allow to fit  $\omega_{\text{max}}$ . This is exemplified in Figure 6a for the bulk system and  $N = 64$ . We therefore focus on the VFT fits in the following.

Figure 6a depicts the  $T$  dependence of  $\omega_{\text{max}}$  for the bulk and film and for  $N = 10$  and 64. While the peak frequencies of the different systems are close to each other at high  $T$ , the curves

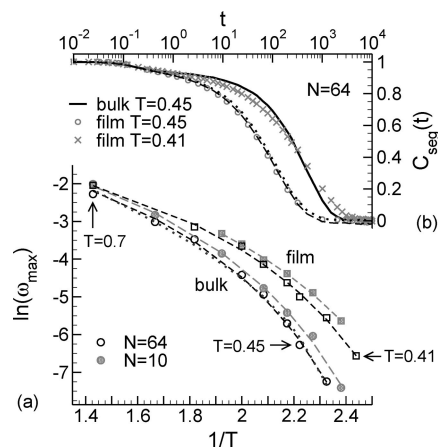


**Figure 6.** (a) Arrhenius plot of the peak frequency  $\omega_{\text{max}}(T)$  of the dielectric loss of the segmental mode for the bulk with  $N = 64$  (open circles) and  $N = 10$  (filled circles) and for a supported film of thickness  $h \sim 7$  ( $h$  changes with temperature<sup>39</sup>) and chain lengths  $N = 64$  (open squares) and  $N = 10$  (filled squares). For all systems the dashed lines represent a fit to the VFT equation (eq 20). The dotted line for the bulk system with  $N = 64$  is a fit to the MCT prediction, eq 19, where the values for  $T_c (=0.415)$  and  $\gamma (=1.96)$  are taken from ref 40. (b) Correlation functions of the segmental mode for  $N = 64$  in the bulk at  $T = 0.45$  (solid line) and in a supported film ( $h = 7.5$ ) at  $T = 0.45$  (circles) and  $T = 0.41$  (crosses). For the film at  $T = 0.45$  the segmental correlation functions parallel (dashed line) and perpendicular (dotted line) to the interfaces are also shown. They agree with the result that is averaged over all directions (circles).

splay out with decreasing temperature, the film being systematically faster than the bulk. This splaying out is reflected by the value of  $T_0$ . The Vogel–Fulcher temperature is lower in the film ( $T_0^{N=64} = 0.293$ ,  $T_0^{N=10} = 0.286$ ) than in the bulk ( $T_0^{N=64} = 0.327$ ,  $T_0^{N=10} = 0.31$ ), and longer chains have a higher  $T_0$  for the same geometry. These trends agree with the ones found for  $T_g$  and  $T_c$  in our previous work<sup>39,40,61</sup> and with experimental results.<sup>3,22,28</sup>

Furthermore, we find that the fits yield for all systems the same  $D \approx 2.5$ .<sup>91</sup> Apparently, confinement mainly affects  $T_0$  but not the fragility of our model glass-former. Although the present simulations are limited to temperatures that are high compared to the experimental  $T_g$ , there is evidence in favor of our result from experiments. For instance, dielectric spectroscopy for the molecular glass-former *N*-methyl- $\epsilon$ -caprolactam confined in pores,<sup>92</sup> thin polymer films of PET,<sup>58</sup> PS,<sup>28</sup> or P2VP,<sup>45</sup> and relaxation dynamics experiments on supported and freely standing PS films<sup>93</sup> suggest that  $T_0$  shifts with increasing confinement, while the fragility does not. (See also ref 59 for further discussion. There are, however, also reports in the literature which find that the fragility decreases with decreasing film thickness.<sup>3,22</sup>)

Figure 6a demonstrates that the difference of the  $\alpha$ -time scales between bulk and film increases with decreasing  $T$ . Thus, it is interesting to compare at low  $T$  the corresponding segmental correlation functions. (For high  $T$  this has already been done in Figure 3.) Figure 6b shows such a comparison for  $T = 0.45$  and  $N = 64$ . We see that, while the bulk  $C_{\text{seg}}(t)$  exhibits a two-step relaxation characteristic of the supercooled melt, this feature is not as pronounced for the film. The film  $C_{\text{seg}}(t)$  rather resembles the bulk relaxation at a temperature higher than  $T = 0.45$  (Figure 5a). The same observation has already been made and discussed in our previous work.<sup>39,61</sup> There, it was also pointed out that a better comparison of the time dependence of correlation functions is possible by eliminating the disparity in the  $\alpha$ -times, that is, by comparing bulk and film dynamics at temperatures where they have similar relaxation times. For  $N = 64$  this condition is fulfilled when comparing the bulk at  $T$



$= 0.45$  to the film at  $T = 0.41$  (Figure 6a). We see from Figure 6b that the film  $C_{\text{seg}}(t)$  exhibits a stronger stretching than the bulk correlation function. Broadening of the  $\alpha$ -relaxation which increases for strong confinement is a characteristic feature of thin glass-forming polymer films.<sup>3,21,28,58</sup> In our case, the broadening is related to the spatial heterogeneity of the film dynamics, as alluded to above, and will be discussed in more detail in section 5.

It is also interesting to test whether confinement induces different segmental relaxations parallel or perpendicular to the plane of the film. In order to study this dependence we introduce the correlation functions

$$C_{\text{seg},x}(t) = \frac{\langle \mu_{\text{seg},x}(t) \mu_{\text{seg},x}(0) \rangle}{\langle |\mu_{\text{seg},x}(0)|^2 \rangle} \quad (x = \perp, \parallel) \quad (21)$$

where  $\mu_{\text{seg},\perp}(t)$  refers to the component of the segmental dipole moment perpendicular to the plane of the film and  $\mu_{\text{seg},\parallel}(t)$  to the component within the plane of the film. The result of this analysis is shown in Figure 6. We see that confinement does not strongly affect the relaxation in different directions. The segmental dynamics of the film is thus (nearly) isotropic.

**4.2. Relaxation of the Normal Mode.** Experimental studies<sup>52–56</sup> suggest that thin films of *cis*-1,4-PI exhibit an additional relaxation mode, a “confinement-induced mode” (CIM),<sup>54,55</sup> between the segmental and the normal mode if the chain length is larger than  $N_e$ .<sup>56</sup> The CIM shows no molecular weight dependence and its relaxation time decreases with decreasing film thickness, while its dielectric strength increases at the expense of that of the normal mode.<sup>54–56</sup>

We have not observed this interesting phenomenon in the present study, neither for  $N = 64$  nor for  $N = 256$  (recall that  $N_e = 32$ ). A possible reason could be as follows: It was suggested<sup>54,55</sup> that the molecular origin of the CIM is related to an immobilization of chain segments in contact with the substrate. This immobilization interrupts the fluctuations of the end-to-end vector so that only terminal subchains remain dielectrically active. Their fluctuations could give rise to the CIM. In our simulations, however, the wall leads to enhanced dynamics relative to the bulk, and so we do not expect to find a CIM.

Nevertheless, further study of the normal mode for long chains could be interesting because the chain dimension is perturbed anisotropically in thin films.<sup>85,94</sup> These perturbations might also be reflected in the relaxation of the normal mode. In analogy to the analysis of the segmental mode we therefore define

$$C_{N,x}(t) = \frac{\langle \mu_{N,x}(t) \mu_{N,x}(0) \rangle}{\langle |\mu_{N,x}(0)|^2 \rangle} \quad (x = \perp, \parallel) \quad (22)$$

where  $\mu_{N,\perp}(t)$  and  $\mu_{N,\parallel}(t)$  refer to the component of the normal-mode dipole moment perpendicular and parallel to the plane of the film, respectively.

Figure 7 shows the results of this analysis. Contrary to  $C_{\text{seg}}(t)$ , we find that the relaxation of the normal mode is anisotropic in the films. The parallel and perpendicular components display the following features: The decay of  $C_{N,\perp}(t)$  is more strongly stretched than that of  $C_{N,\parallel}(t)$ , and  $C_{N,\perp}(t)$  relaxes more rapidly than  $C_{N,\parallel}(t)$ . Partially the latter finding might be due to the fact that the perpendicular component of the end-to-end vector  $R_{e,y}$  is on average smaller than the in-plane components  $R_{e,x}$  and  $R_{e,z}$ . Since a shorter vector can reorient faster,  $C_{N,\parallel}(t)$  should decay more rapidly. For the total correlation function of the normal mode  $C_N(t)$ —which is, in analogy to  $C(t)$  of eq 15, the weighted sum of  $C_{N,\perp}(t)$  and  $C_{N,\parallel}(t)$ —the fast relaxation in the  $y$ -direction does not play an important role since its amplitude is proportional to  $R_{e,y}^2$ , which is about 3 times smaller than the

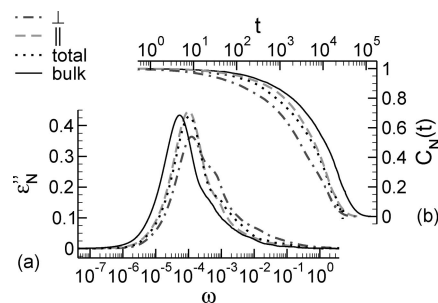


**Figure 7.** Dielectric loss (a) and time correlation function (b) of the normal mode. The solid line indicates the bulk behavior at  $T = 0.7$  for chains of length  $N = 64$ . For the same  $T$  and  $N$  the other lines represent the results obtained from a film of thickness  $h = 7.5$  for the total correlation function of the normal mode ( $C_N(t)$  and  $\epsilon''_N(\omega)$ ; dotted lines) and its decomposition into components parallel ( $C_{N,\parallel}(t)$  and  $\epsilon''_{N,\parallel}(\omega)$ ; dashed lines) and perpendicular ( $C_{N,\perp}(t)$  and  $\epsilon''_{N,\perp}(\omega)$ ; dash-dotted lines) to the plane of the film.

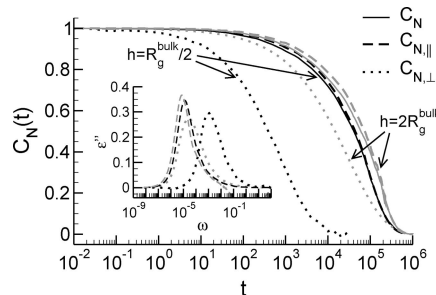


**Figure 8.** Correlation functions of the normal mode (main figure) and corresponding dielectric loss spectra (inset) for  $N = 256$  at  $T = 1$ . The data shown represent results for films of two thicknesses,  $h = 4 \approx R_g^{\text{bulk}}/2$  (black lines) and  $h = 17 \approx 2R_g^{\text{bulk}}$  (gray lines), where  $R_g^{\text{bulk}}$  is the bulk radius of gyration. In the main figure, three correlation functions are compared for each  $h$ , the component of the normal mode parallel to the plane of the film (dashed lines), perpendicular to (dotted lines), and the total correlation function of the film (full lines). In the inset, the dielectric spectra obtained from the components parallel (dashed lines) and perpendicular (dotted lines) to the plane of the film are shown.

average in-plane component  $R_{e,xz}$ . Thus,  $C_{N,\parallel}(t)$  dominates the total correlation function  $C_N(t)$ .

This effect may be expected to become stronger for smaller film thickness or longer chains. Figure 8 tests this idea by extending the analysis to  $N = 256$ . For this case study we performed simulations at a higher temperature  $T = 1$  and investigated two different film thicknesses,  $h = 17 \approx 2R_g^{\text{bulk}}$  and  $h = 4 \approx (R_g^{\text{bulk}} = 8.2)$ . Indeed, for  $h = 4$  the relaxation times of the normal mode in parallel and perpendicular directions are well separated. As expected, the contribution of  $C_{N,\perp}(t)$  to  $C_N(t)$  is very weak, since the ratio  $[(R_{e,y} = 3)/(R_{e,xz} = 18.6)]^2 \sim 0.02$  is so small that the relaxation of the total correlation function is fully determined by the in-plane process  $C_{N,\parallel}(t)$ .

## 5. Segmental Correlation Function: Layer-Resolved Analysis

In previous sections we mentioned that the film dynamics is spatially heterogeneous because it depends on the distance from the interfaces. In order to quantify this effect, it is necessary to determine layer-resolved correlation functions of the dipole moment. While this is quite easily possible for the segmental dipole moment due to its local character, it is not obvious how to define such a function for the normal mode. Therefore, we focus on the segmental mode in the following.

We introduce a local segmental dipole moment  $\mu_{\text{seg}}^{\text{sol}}(y)$  in the following way: Consider a layer of width  $\Delta y$  at distance  $y$  from



the supporting wall. For this layer we find all monomers whose contiguous bonds lie within  $\Delta y/2$  from  $y$  and associate a perpendicular dipole moment with each of these monomers according to eq 5. More precisely, we define

$$\mathbf{t}_j^a(y) = \begin{cases} (-1)^a(\mathbf{b}_j^a - \mathbf{b}_j^{a-1}) \left| \frac{y_j^a + y_j^{a+1}}{2} - y \right| < \frac{\Delta y}{2} \\ 0 & \text{else} \end{cases} \quad (23)$$

where  $y_j^a$  denotes the  $y$ -coordinate of monomer  $a$  on chain  $j$ . Following eqs 6–9 this allows us to introduce a layer-resolved segmental dipole moment

$$\boldsymbol{\mu}_{\text{seg}}^{\text{col}}(y, t) = \boldsymbol{\mu}_{\text{seg}} \sum_{j=1}^n \sum_{a=2}^{N-1} \mathbf{t}_j^a(y, t) \quad (24)$$

and, using eq 12, its autocorrelation function

$$C_{\text{seg}}^{\text{col}}(y, t) = \frac{\langle \boldsymbol{\mu}_{\text{seg}}^{\text{col}}(y, t) \cdot \boldsymbol{\mu}_{\text{seg}}^{\text{col}}(y, 0) \rangle}{\langle |\boldsymbol{\mu}_{\text{seg}}^{\text{col}}(y, 0)|^2 \rangle} \quad (25)$$

This function is shown in Figure 9 for  $T = 0.4$  and  $N = 64$ . We find that the dynamics is spatially heterogeneous: In the center of the film ( $y = 8$ ) the relaxation of  $C_{\text{seg}}^{\text{col}}(y, t)$  is bulklike; the relaxation accelerates continuously as the interfaces are approached; and this acceleration is stronger at the free surface ( $y = 15$ ) than at the supporting wall ( $y = 1$ ).

These findings agree with the results from our previous analyses for the mean-square displacement of all monomers and incoherent scattering function.<sup>39,40,61</sup> But while the mean-square displacement and incoherent scattering function are single-particle quantities, this is not the case for the total dipole moment; it is a collective property of the system. By summing only over dipole moments spanned by bonds that are situated within a layer, a different subset is chosen every time when we calculate the local segmental mode. Therefore, a partial decorrelation occurs due to the appearance or disappearance of segmental dipoles as they move in or out of the layer. This leads to a slightly lower plateau of  $C_{\text{seg}}^{\text{col}}(y, t)$  in the film center compared to the bulk correlation function.

Furthermore, the exact height of the plateau depends on the choice of the layer thickness  $\Delta y$ . We chose  $\Delta y = 2$  because the average correlation function of the film,  $C_{\text{seg}}^{\text{col}}(t)$ , is then approximated well by the arithmetic mean over the layer-resolved correlation functions. On the one hand, this indicates that cross-correlations between the polarization of different layers are negligible;  $C_{\text{seg}}^{\text{col}}(y, t)$  thus provides an accurate picture of the local relaxation in the film. On the other hand, this demonstrates that the film averaged segmental correlation

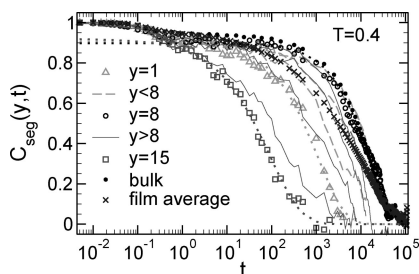


**Figure 9.** Layer-resolved correlation function of the segmental mode  $C_{\text{seg}}^{\text{col}}(y, t)$  for a film of thickness  $h = 14$  at  $T = 0.4$ . Full lines indicate  $C_{\text{seg}}^{\text{col}}(y, t)$  in layers close to the free surface ( $y > 8$ ); dashed lines indicate  $C_{\text{seg}}^{\text{col}}(y, t)$  close to the supporting surface ( $y < 8$ ). Squares, triangles, and open circles are respectively the results for  $C_{\text{seg}}^{\text{col}}(y, t)$  at the free surface, at the supported surface, and in the film center. Filled circles show the segmental mode in the bulk, and crosses show the segmental mode averaged over the whole film. The dotted lines are fits to eq 26.

aggregates contributions from fast relaxing regions close to the interfaces and bulklike regions near the center of the film. It is this spatial heterogeneity of the dynamics which leads to the stronger stretching of the average segmental mode in the film relative to the bulk. Similar conclusions are also drawn from other simulations<sup>63,95</sup> and experiments.<sup>3,58</sup>

The previous discussion may be corroborated by a quantitative analysis. We fit the final decay of  $C_{\text{seg}}^{\text{col}}(y, t)$  by the stretched exponential

$$C_{\text{seg}}^{\text{col}}(y, t) = a(y) e^{-(t/\tau_{\text{seg}}(y))^{\beta(y)}} \quad (26)$$

The results are summarized in Figure 10. We see that, as the interfaces are approached, the stretching of the relaxation function increases (lower value of  $\beta$ ) while the relaxation time decreases. These deviations from bulk behavior, which prevails in the center of the film, occur gradually and are more pronounced at the free surface than at the supporting wall. Our results are thus consistent with the idea that interfaces induce smooth gradients in relaxation, the extent of which depends on the nature of the interface. Similar conclusions are drawn from simulations of confined glass-forming liquids<sup>63</sup> and polymer melts<sup>95</sup> and from experiments on fluorescent multilayer polymer films<sup>26,96</sup> (see e.g. ref 61 for a review).

## 6. Discussion: Relation to Experiment

The discussion of section 4 leads to a natural question: How may the simulated dielectric spectra for thin films be related to experimental results from broadband dielectric spectroscopy? Here we attempt to give an answer to this question by focusing on the  $\alpha$ -relaxation. Our starting point is that experiments measure the segmental relaxation as the system's response to an external electric field ( $E$ ). On the basis of the results from section 5 we suggest to model the  $\alpha$ -relaxation of a film by a system of capacitors. This model—an extension of the work of ref 58—is tentative but allows us to account for the electric field as the stimulus of dielectric relaxation in experiments. Our model makes the interesting proposition that the direction of the  $E$ -field relative to the plane of the film might have an important influence on the dielectric spectra. In the following we explain this idea and explore some of its consequences.

**6.1. Dielectric Function in Thin Films: Modeling by a System of Capacitors.** The results of section 5 for the layer-resolved segmental mode exemplified the spatial heterogeneity of the film dynamics: The film can be decomposed into  $n_l (= h/\Delta y)$  layers, each of thickness  $\Delta y$ , and the segmental correlation function  $C_{\text{seg}}^{\text{col}}(y_i, t)$  depends on the position  $y_i$  ( $i = 1, \dots, n_l$ ) of the layer from the supporting wall. Through the FDT we can associate a layer-dependent complex dielectric function with this segmental mode

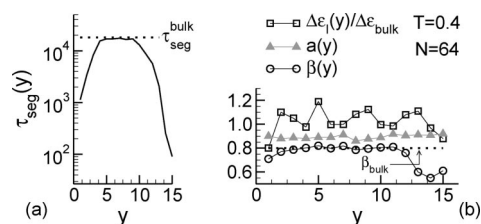


**Figure 10.** Layer dependence of the fit results to eq 26 for a supported film of thickness  $h = 14$  at  $T = 0.4$ . In both figures  $y$  represents the distance from the supporting wall. (a) Relaxation time  $\tau_{\text{seg}}(y)$  of the segmental mode.  $\tau_{\text{seg}}^{\text{bulk}}$  denotes the corresponding bulk value. (b) Amplitude  $a(y)$  and stretching exponent  $\beta(y)$ . The figure also shows the ratio  $\Delta\epsilon_l(y)/\Delta\epsilon_{\text{bulk}}$  given by eq 35. Here  $\Delta\epsilon_l(y)$  is the layer-dependent dielectric strength of the segmental mode when the electric field is applied perpendicular to the plane of the film, and  $\Delta\epsilon_{\text{bulk}}$  is the dielectric strength of the segmental mode in the bulk.

$$\frac{\varepsilon^*(\omega, y_i) - \varepsilon_\infty}{\Delta\varepsilon(y_i)} = -F \left[ \frac{\partial}{\partial t} C_{\text{seg}}^{\text{col}}(y_i, t) \right] \quad (27)$$

where  $\Delta\varepsilon(y_i)$  denotes the dielectric strength of the layer  $i$  and we assumed that  $\varepsilon_\infty$  remains constant.

The function  $\varepsilon_i^* = \varepsilon^*(\omega, y_i)$  is the generalization of the dielectric constant of a nonconducting medium. The dielectric constant in turn is related to the capacitance  $C_i$  of a capacitor by a result from electrostatics:  $C_i \propto \varepsilon_i^* A/l$ , where  $A$  is the area of the plates of the capacitor and  $l$  is the spacing between them. This suggests that we may think of the film as being a system of  $n_l$  ideal capacitors (with zero resistance at the electrodes)<sup>97</sup> which can be connected in series or in parallel. It is at that point where the direction of the  $E$ -field will matter.

To see this, we consider two setups (Figure 11). The first setup, called setup I in the following, corresponds to the usual experimental situation that the  $E$ -field is perpendicular to the plane of the film. A configuration allowing for a parallelly oriented  $E$ -field is much more difficult to realize in experiments. We refer to this setup as setup II. Depending on the direction of the  $E$ -field the measured average dielectric response  $\varepsilon^*(\omega, h)$  for a film of thickness  $h$  is expected to be different:

**Setup I.** The  $E$ -field is perpendicular to the plane of the film. In the language of a system of capacitors this implies that the external voltage is applied at the first capacitor (layer in contact with the supporting wall) and at the last capacitor (layer at the free surface). Thus, only the sum of the voltages of the  $n_l$  capacitors needs to equal the external voltage. This means that the capacitors are arranged in series. For this arrangement the total capacitance  $C$  is given by  $C^{-1} = \sum_{i=1}^{n_l} C_i^{-1}$ . Using  $C \propto \varepsilon_i^*(\omega, h) L^2/h$  and  $C_i \propto \varepsilon_i^* L^2/\Delta y$  (Figure 11), we find ( $n_l = h/\Delta y$ )

$$\frac{1}{\varepsilon_i^*(\omega, h)} = \frac{1}{n_l} \sum_{i=1}^{n_l} \frac{1}{\varepsilon^*(\omega, y_i)} \quad (28)$$

**Setup II.** The  $E$ -field is parallel to the plane of the film. This corresponds to a parallel arrangement of the capacitors because the same voltage is applied at each capacitor. In this case the total capacitance is given by  $C = \sum_{i=1}^{n_l} C_i$ . Using  $C \propto \varepsilon_{\text{II}}^*(\omega, h) (Lh)/L$  and  $C_i \propto \varepsilon_i^* (L\Delta y)/L$  (Figure 11), we find

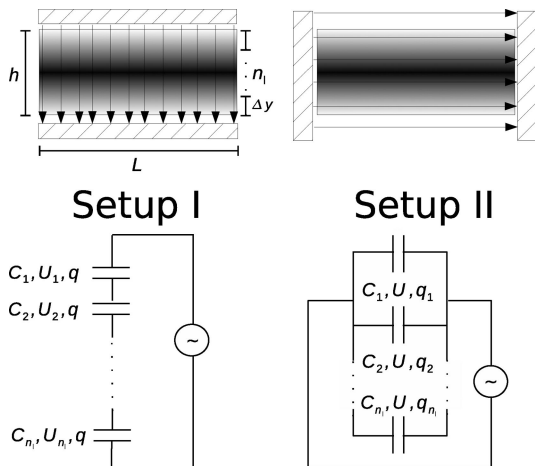


**Figure 11.** Two possible setups: In setup I the electric field (arrows) is perpendicular to the plane of the film, whereas it is parallel in setup II. If we decompose a film of thickness  $h$  into  $n_l$  layers of size  $\Delta y$  and associate with each layer  $i$  a capacitor with capacitance  $C_i$ , the capacitors are arranged in series for setup I and in parallel for setup II. The corresponding circuits are indicated ( $U$  = voltage,  $q$  = electrical charge).

$$\varepsilon_{\text{II}}^*(\omega, h) = \frac{1}{n_l} \sum_{i=1}^{n_l} \varepsilon^*(\omega, y_i) \quad (29)$$

Recalling the discussion of section 5, we then see that the simulated loss spectra of section 4 correspond to setup II:  $C_{\text{seg}}^{\text{col}}(t)$  is the sum of the layer-resolved correlation functions  $C_{\text{seg}}^{\text{col}}(y_i, t)$ , which leads to eq 29 via the FDT. The prevailing experimental situation, however, is setup I. Therefore, the question arises of whether the different averaging procedures implied by eqs 28 and 29 entail significant differences in the results for  $\varepsilon^*(\omega, h)$ .

The answer to this question depends on the value of  $\Delta\varepsilon(y_i)$  and  $\varepsilon_\infty$ . If  $\varepsilon_\infty$  is large relative to  $\Delta\varepsilon(y_i)$  so that the inequality  $\Delta\varepsilon(y_i)/\varepsilon_\infty \ll 1$  holds for all layers, it can be shown from eqs 28 and 29 that the spectra from both setups are identical. This could be the case for polymers with weak dipole moments, such as PS or PI. For polar polymers such as PVAc, however, the difference between both setups may be large.

To obtain a better insight into possible differences, the next sections explore consequences of eqs 28 and 29 by numerically computing  $\varepsilon_I(\omega, h)$  and  $\varepsilon_{\text{II}}(\omega, h)$  for three model situations.

**6.2. Case Study I: Fast Relaxation in the Film without Preferential Orientation of Segmental Dipoles.** Based on the results of section 5 for the layer-resolved analysis of the segmental dynamics, this first case study employs the following assumptions:

1. We only consider the  $\alpha$ -relaxation of the segmental mode which is described by the stretched exponential of eq 26. Since the amplitude  $a(y)$  in eq 26 is almost independent of  $y$  and close to 1 (Figure 10), we choose  $a(y) = 1$  here. Following eq 27 the layer-dependent complex dielectric response function is then given by

$$\frac{\varepsilon^*(\omega, y) - \varepsilon_\infty}{\Delta\varepsilon(y)} = -F \left[ \frac{\partial}{\partial t} \exp \left[ - \left( \frac{t}{\tau_{\text{seg}}(y)} \right)^{\beta(y)} \right] \right] \quad (30)$$

The values for  $\tau_{\text{seg}}(y)$  and  $\beta(y)$  are taken from Figure 10.

2. The second assumption concerns the dielectric strength. Quite generally, the dielectric strength is proportional to the mean-square total dipole moment in direction of the  $E$ -field,  $\langle \mu_{\text{seg}, E}^{\text{col}}(0)^2 \rangle$ .<sup>87</sup> For the bulk this relation reads

$$\Delta\varepsilon_{\text{bulk}} \propto \frac{\langle \mu_{\text{seg}, E}^{\text{col}}(0)^2 \rangle}{V} = \frac{\langle \mu_{\text{seg}}^{\text{col}}(0)^2 \rangle}{3V} \quad (31)$$

where  $V$  is the volume of the system. The last equality holds because all spatial directions are equivalent in the bulk. For thin films, however, the introductory discussion of this section suggests that we should distinguish between the  $E$ -field applied perpendicular (setup I) and parallel (setup II) to the plane of the film. Accordingly, we split the layer-dependent dielectric strength into perpendicular ( $\Delta\varepsilon_I$ ) and parallel ( $\Delta\varepsilon_{\text{II}}$ ) components. We write

$$\Delta\varepsilon(y) = \Delta\varepsilon_I(y) + 2\Delta\varepsilon_{\text{II}}(y) = 3\Delta\varepsilon_{\text{bulk}} \quad (32)$$

In this case study we assume that  $\Delta\varepsilon(y)$  is independent of  $y$ , i.e.

$$\Delta\varepsilon_I(y) = \Delta\varepsilon_{\text{II}}(y) = \Delta\varepsilon_{\text{bulk}} \quad (33)$$

and we pose  $\Delta\varepsilon_{\text{bulk}} = 1$  for numerical applications.

Equation 33 may be justified by the following argument: In our system the interfaces do not lead to strong orientations of the bonds. Thus, the trimers spanning  $\mathbf{t}_j^0$  are not preferentially parallel to the plane of the film. This should imply that the component of the layer-dependent total dipole moment perpendicular to the interfaces,  $\langle \mu_{\text{seg}, I}^{\text{col}}(y, 0)^2 \rangle$ , is proportional to the total dipole moment in the bulk,  $\langle \mu_{\text{seg}}^{\text{col}}(0)^2 \rangle$ . More precisely, we should have

$$\langle |\mu_{\text{seg},I}^{\text{col}}(y, 0)|^2 \rangle \approx \frac{1}{n_l} \frac{\langle |\mu_{\text{seg}}^{\text{col}}(0)|^2 \rangle}{3} \quad (34)$$

Due to eq 31 we then expect that

$$\frac{\Delta \varepsilon_I(y)}{\Delta \varepsilon_{\text{bulk}}} = \frac{n_l \langle |\mu_{\text{seg},I}^{\text{col}}(y, 0)|^2 \rangle}{\langle |\mu_{\text{seg}}^{\text{col}}(0)|^2 \rangle / 3} \approx 1 \quad (35)$$

Within the statistical uncertainties this expectation is confirmed in Figure 10.

3. We choose

$$\varepsilon_{\infty} = 0 \quad (36)$$

This is, of course, a hypothetical value. We make this choice here to eliminate the impact of  $\varepsilon_{\infty}$  on the spectra resulting from eqs 28 and 29. For setup II,  $\varepsilon_{\infty}$  is just an additive constant, but for setup I it is folded in the spectra in a complicated way (cf. Appendix). Choosing  $\varepsilon_{\infty} = 0$  will make the comparison of both setups more transparent.

Using these assumptions, we calculate the real and imaginary parts of the dielectric function for setup I (eq 28) and setup II (eq 29). Figure 12 displays the results. We clearly see that the spectra depend on the setup. For both setups the peak frequency  $\omega_{\text{max}}$  of  $\varepsilon''(\omega)$  shifts with decreasing film thickness to larger values relative to the bulk (Figure 12a). This reflects the acceleration of the film dynamics discussed before. The shift of  $\omega_{\text{max}}$  is nearly independent of the setup; the shape of  $\varepsilon'(\omega)$  and  $\varepsilon''(\omega)$ , however, strongly depends on it.

Qualitatively, we may understand this impact on the shape by the following argument. Let us assume that the layer-dependent segmental mode exhibits a Debye relaxation,  $C_{\text{seg}}^{\text{col}}(y_i, t) = \exp[-t/\tau_{\text{seg}}(y_i)]$ . The results of the Appendix then show that the loss spectra of setups I and II agree with each other for  $\omega \rightarrow 0$  but differ for  $\omega \rightarrow \infty$  because the high-frequency wing is determined by different averages of the local segmental relaxation time. More precisely, we find from eqs 65–69

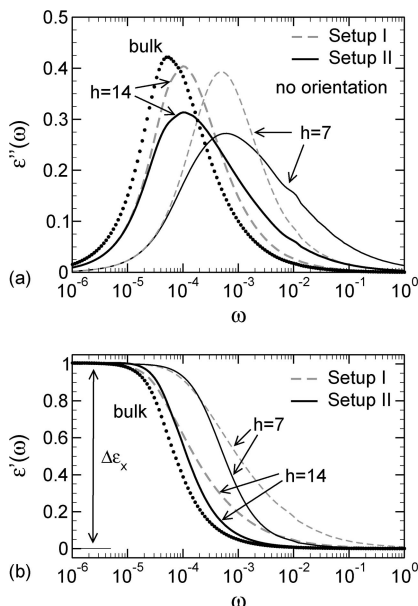


**Figure 12.** (a) Imaginary part of the dielectric function calculated according to eq 28 (setup I, gray dashed lines) and eq 30 (setup II, black solid lines) for supported films of thickness  $h = 7$  and  $h = 14$  at  $T = 0.4$  and for  $N = 64$ . The filled circles indicate the bulk results. To calculate these spectra the assumptions of eqs 30–36 are used. In particular, eq 33 implies that the orientation of segmental dipoles remains bulklike throughout the film (“no orientation”). (b) Corresponding real part of the dielectric function. The dielectric strength  $\Delta \varepsilon_x$  is indicated. It is the same for both setups ( $x = \text{I, II}$ ) and equal to the bulk value  $\Delta \varepsilon_{\text{bulk}} = 1$ .

$$\varepsilon_I''(\omega \rightarrow 0) = \varepsilon_{\text{II}}''(\omega \rightarrow 0) = \omega \langle \tau_{\text{seg}} \rangle \quad (37)$$

whereas

$$\begin{aligned} \varepsilon_I''(\omega \rightarrow \infty) &= \frac{1}{\omega} \frac{1}{\langle \tau_{\text{seg}} \rangle} \\ \varepsilon_{\text{II}}''(\omega \rightarrow \infty) &= \frac{1}{\omega} \left\langle \frac{1}{\tau_{\text{seg}}} \right\rangle \end{aligned} \quad (38)$$

with

$$\begin{aligned} \langle \tau_{\text{seg}} \rangle &= \frac{1}{n_l} \sum_{i=1}^{n_l} \tau_{\text{seg}}(y_i) \\ \left\langle \frac{1}{\tau_{\text{seg}}} \right\rangle &= \frac{1}{n_l} \sum_{i=1}^{n_l} \frac{1}{\tau_{\text{seg}}(y_i)} \end{aligned} \quad (39)$$

Looking back at Figure 10a, we may expect that  $\langle \tau_{\text{seg}}^{-1} \rangle > \langle \tau_{\text{seg}} \rangle^{-1}$  because the short relaxation times at the interfaces give an important contribution to  $\langle \tau_{\text{seg}}^{-1} \rangle$ . Indeed,  $\langle \tau_{\text{seg}}^{-1} \rangle \approx 10 \langle \tau_{\text{seg}} \rangle^{-1}$  for the data shown in Figure 10a. For a Debye relaxation we thus find that  $\varepsilon_{\text{II}}''(\omega) > \varepsilon_I''(\omega)$  for large  $\omega$ .

Therefore, the preceding analysis suggests that  $\varepsilon_{\text{II}}''(\omega)$  agrees with  $\varepsilon_I''(\omega)$  at low frequencies but is larger than  $\varepsilon_I''(\omega)$  at high frequencies. This is what we observe in Figure 12a. This difference between both setups also implies that the peak height  $\varepsilon_{\text{II}}''(\omega_{\text{max}})$  must be smaller than that of  $\varepsilon_I''(\omega_{\text{max}})$  due to the sum rule<sup>87</sup>

$$\frac{2}{\pi} \int_0^\infty d\omega \frac{\varepsilon_x''(\omega)}{\omega} = \Delta \varepsilon_x = \varepsilon_x'(\omega \rightarrow 0) - \varepsilon_{\infty} \quad (x = \text{I, II}) \quad (40)$$

and our choice  $\Delta \varepsilon_x = 1$  for both setups (Figure 12b).

### 6.3. Case Study II: Fast Relaxation in the Film with Preferential Orientation of Segmental Dipoles.

In addition to a broadening of the  $\alpha$ -relaxation, a further feature that is commonly observed in experiments is a decrease of the dielectric strength of the  $\alpha$ -peak with decreasing film thickness.<sup>3,22,28,58</sup> This decrease is often explained in terms of a “dead layer”<sup>3,21</sup> of immobilized dipoles at the supporting electrode, possibly followed by a layer with reduced segmental mobility.<sup>30,58</sup> Absence or strong reduction of molecular mobility on the time scale of the dynamic glass transition implies that the dipoles in these layers do not or only weakly contribute to the  $\alpha$ -process, thus leading to a decrease of the dielectric strength. Such an impact on the molecular mobility can occur from strong adsorption of the chains at the electrode.<sup>45,58</sup>

However, even without invoking a slowing down of mobility it is possible to obtain a decrease of the dielectric strength if we assume a preferential orientation of segmental dipoles near the electrode(s). For instance, if the dipoles tend to align parallel to the electrode(s), the dielectric strength should decrease for setup I because the dipoles are preferentially perpendicular to the  $E$ -field, and this orientation makes them “invisible” in setup I. However, they are “visible” in setup II where the field is parallel to the plane of the film.

This second case study focuses on such orientational effects by the following assumptions:

1. We keep the first assumption of case study I, i.e., eq 30.
2. Instead of eq 33, the local dielectric strength must now depend on distance to reflect the propensity of the dipoles to orient parallelly on approaching the supporting wall. For setup I this implies that  $\Delta \varepsilon_I(y)$  is small at the wall and increases toward  $\Delta \varepsilon_{\text{bulk}}$  with increasing  $y$ . To model this trend, we assume that  $\Delta \varepsilon_I(y)$  is 0.25 at  $y = 1$  and increases linearly to the bulk value within four monomer diameters. For larger distances up to the free surface we assume that  $\Delta \varepsilon_I(y)$  stays bulklike. More precisely



$$\Delta\epsilon_I(y) = \begin{cases} \frac{3}{4}y - \frac{1}{2} & 1 \leq y < 4 \\ \Delta\epsilon_{\text{bulk}} = 2.5 & 4 \leq y \leq h \end{cases} \quad (41)$$

( $\Delta\epsilon_{\text{bulk}} = 2.5$  is typical of polar polymers.<sup>76</sup>) If we use eq 32, eq 41 implies for setup II that the dielectric strength decreases with increasing distance from the wall

$$\Delta\epsilon_{II}(y) = \begin{cases} 4 - \frac{3}{8}y & 1 \leq y < 4 \\ \Delta\epsilon_{\text{bulk}} = 2.5 & 4 \leq y \leq h \end{cases} \quad (42)$$

Note that by imposing eq 32, i.e.,  $\Delta\epsilon(y) = 3\Delta\epsilon_{\text{bulk}}$ , we assume that the components perpendicular ( $\Delta\epsilon_I$ ) and parallel ( $2\Delta\epsilon_{II}$ ) to the wall add up to the bulk value for all layers. A possible dependence of  $\Delta\epsilon(y)$  on the distance from the wall is neglected.

3. We choose

$$\epsilon_{\infty} = 2.5 \quad (43)$$

This is a typical value for nonpolar polymers, such as PI or polybutadiene,<sup>77,82</sup> and for Lennard-Jones systems.<sup>98</sup>

Figure 13 shows the real and imaginary parts of the dielectric function which result from these assumptions. We see that the dielectric spectra differ considerably from those of case study I, although the same segmental relaxation function, eq 30, was used in both studies. This hints at the importance of  $\Delta\epsilon(y)$  and  $\epsilon_{\infty}$  in determining the dielectric response of the film. Insight into this influence can again be obtained by assuming a Debye relaxation for each layer (Appendix). To illustrate trends, we restrict the discussion to the low-frequency limit. This limit yields, contrary to case study I (eq 37), differences between setup I and II. For setup I we find (see eqs 62–64)

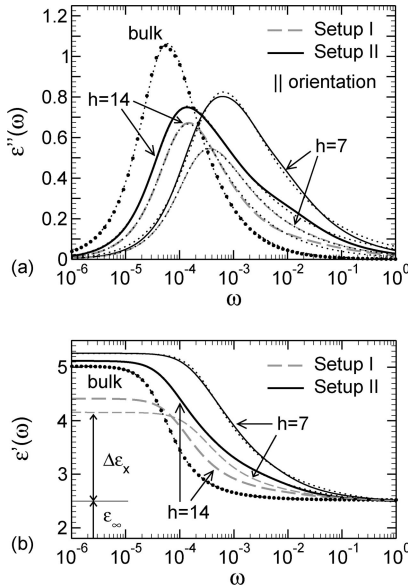


**Figure 13.** (a)  $\epsilon''(\omega)$  following from eq 28 (setup I, gray dashed lines) and eq 29 (setup II, black solid lines) for supported films of thickness  $h = 7$  and  $h = 14$  at  $T = 0.4$  and for  $N = 64$ . The filled circles indicate the bulk results. The calculation of the spectra employs the assumptions of eqs 30–36. In particular, eq 33 implies that the segmental dipoles tend to orient parallel to the supporting wall as the wall is approached (“|| orientation”). The dotted lines indicate fits to the HN function, eq 48; the fit results are compiled in Table 1. (b) Corresponding real part of the dielectric function. The value of  $\epsilon_{\infty}$  and an example for the dielectric strength  $\Delta\epsilon_x$  ( $x = I, II$ ),  $\Delta\epsilon_I(h = 7)$ , are indicated.

$$\epsilon'_I(\omega \rightarrow 0) = \left[ \frac{1}{n_I} \sum_{i=1}^{n_I} \frac{1}{\epsilon_{\infty} + \Delta\epsilon(y_i)} \right]^{-1} \quad (44)$$

$$\epsilon''_I(\omega \rightarrow 0) = \left[ \frac{1}{n_I} \sum_{i=1}^{n_I} \frac{1}{\epsilon_{\infty} + \Delta\epsilon(y_i)} \right]^{-2} \left[ \frac{1}{n_I} \sum_{i=1}^{n_I} \frac{\tau_{\text{seg}}(y_i) \Delta\epsilon(y_i)}{\epsilon_{\infty} + \Delta\epsilon(y_i)} \right] \omega \quad (45)$$

and for setup II

$$\epsilon'_{II}(\omega \rightarrow 0) = \epsilon_{\infty} + \frac{1}{n_{II}} \sum_{i=1}^{n_{II}} \Delta\epsilon(y_i) \quad (46)$$

$$\epsilon''_{II}(\omega \rightarrow 0) = \left[ \frac{1}{n_{II}} \sum_{i=1}^{n_{II}} \tau_{\text{seg}}(y_i) \Delta\epsilon(y_i) \right] \omega \quad (47)$$

These results allow us to interpret qualitative features of the spectra shown in Figure 13. For instance, eqs 45 and 47 suggest that, contrary to case study I, the loss spectra of both setups need not coincide at small  $\omega$ —this is borne out by our data (Figure 13a)—and that the time scale on which the dielectric loss vanishes depends explicitly on  $\epsilon_{\infty}$  in setup I, whereas it is independent of  $\epsilon_{\infty}$  for setup II. Furthermore, we also understand why the loss peak for  $h = 7$  is bigger in setup II than in setup I. According to eq 40, the area under loss peak is related to the dielectric strength, and Figure 13b reveals that  $\Delta\epsilon_I(h = 7) < \Delta\epsilon_{II}(h = 7)$ . (The values of  $\Delta\epsilon_I$  and  $\Delta\epsilon_{II}$  can be calculated if we insert eq 41 in eq 44 and eq 42 in eq 46.)

For further, more quantitative analysis we fit our data to a Havriliak/Negami (HN) function (dotted lines in Figure 13; the decomposition into real and imaginary parts can be found on page 62 of ref 87)

$$\epsilon^*(\omega) = \epsilon_{\infty} + \frac{\Delta\epsilon}{[1 + (i\omega\tau_{\text{HN}})^{\beta_{\text{HN}}}]^{\gamma_{\text{HN}}}} \quad (48)$$

The exponents  $\beta_{\text{HN}}$  and  $\gamma_{\text{HN}}$  describe respectively the symmetric and asymmetric broadening of  $\epsilon^*(\omega)$ . They satisfy the inequality  $0 < \beta_{\text{HN}}, \beta_{\text{HN}}\gamma_{\text{HN}} \leq 1$  and can be obtained, e.g., from the limiting behavior of  $\epsilon''(\omega)$  at low and high frequencies:<sup>87</sup>

$$\epsilon''(\omega) \sim \omega^{\beta_{\text{HN}}} \quad \text{for } \omega \ll 1/\tau_{\text{HN}} \quad (49)$$

$$\epsilon''(\omega) \sim \omega^{\beta_{\text{HN}}\gamma_{\text{HN}}} \quad \text{for } \omega \gg 1/\tau_{\text{HN}} \quad (50)$$

The results of the HN fit are summarized in Table 1. We find that  $\beta_{\text{HN}}$  is nearly 1 for both film thicknesses and setups. This must be so because the definition of complex dielectric function, eq 18, implies  $\epsilon''(\omega) \sim \omega$  for  $\omega \rightarrow 0$ . On the other hand, the high-frequency behavior of the dielectric loss reflects the different broadening of the spectra. This broadening depends on film thickness and setup. For the same  $h$  we find that setup II leads to broader spectra than setup I.

**6.4. Case Study III: Slow Segmental Relaxation in the Film.** In our system, both the free surface and the smooth supporting wall lead to a speed-up of the relaxation dynamics.

**Table 1. Parameters Extracted from a Fit of Eq 48 to the Data Shown in Figure 13 (Case Study II)<sup>a</sup>**

parameters	setup I ( $h = 14$ )	setup I ( $h = 7$ )	setup II ( $h = 14$ )	setup II ( $h = 7$ )	bulk
$\tau_{\text{HN}}$	12000	5500	16500	3200	22500
$\gamma_{\text{HN}}$	0.50	0.44	0.35	0.46	0.70
$\beta_{\text{HN}}$	1.0	0.98	0.97	0.88	1.0
$\beta_{\text{HN}}\gamma_{\text{HN}}$	0.50	0.43	0.34	0.41	0.70
$\Delta\epsilon$	1.9	1.7	2.7	2.9	2.5
$\omega_{\text{max}}$	$1.5 \times 10^{-4}$	$3.7 \times 10^{-4}$	$1.4 \times 10^{-4}$	$6.5 \times 10^{-4}$	$5.5 \times 10^{-5}$

<sup>a</sup> These data refer to supported polymer ( $N = 64$ ) films ( $h = 14$  and  $h = 7$ ) at  $T = 0.4$  and to the bulk at the same temperature. The last line of the table gives the values  $\omega_{\text{max}}$  of the peak position of the dielectric loss.



By contrast, experimental measurements of  $T_g^{5,6,14,20,25,44}$  and dielectric spectroscopy studies<sup>58</sup> indicate that the presence of attractive substrate interactions can reduce the mobility of polymer segments relative to the bulk. This can lead to a slowing down of the  $\alpha$ -relaxation and, along with that, to an increase of  $T_g$ . A similar slowing down of the relaxation is also found in simulations if the particle–wall interaction is strong. Here, the term “particle–wall interaction” has two meanings:<sup>61</sup> (i) It can mean the direct particle–wall attraction. Large enough attraction can entail slow dynamics.<sup>37,64,65,95,99</sup> (ii) Or it means surface topography. Even without preferential attraction the dynamics may be strongly slowed down if particles become caged in cavities of the substrate.<sup>62,63,100</sup>

In this third case study, we thus extend our modeling to the situation where the walls decelerate the relaxation relative to bulk. Our approach employs ideas from simulations of a glass-forming binary mixture confined between two amorphous walls;<sup>62,63</sup> it is based on the following assumptions:

1. References 62 and 63 study segmental dynamics by the incoherent intermediate scattering function  $\phi_q^s(t)$  for the wave vector  $\mathbf{q}$  corresponding to the maximum of the static structure factor. For this quantity the following observations are made: (i) Near the walls the local dynamics is by orders of magnitude slower than in the center of the film. The slow relaxation continuously turns into bulklike relaxation with increasing distance from the wall. (ii) A layer-resolved analysis of  $\phi_q^s(t)$  suggests that the  $\alpha$ -relaxation is stretched and the stretching increasing from the film center, where it is bulklike, to the wall.

Observation i was quantified in refs 62 and 63 by introducing an empirical formula for the  $y$  dependence of the segmental relaxation time

$$\ln\left(\frac{\tau_{\text{seg}}(y)}{\tau_{\text{seg}}^{\text{bulk}}}\right) = A[e^{-y/\xi} + e^{-(D-y)/\xi}] \quad (51)$$

Here  $D$  denotes the distance between the confining walls, and the length scale  $\xi$  and the amplitude  $A$  are fit parameters. In our modeling we adopt eq 51 with the following choices: (i) We take  $D = 15$  for the position of the upper wall; this leads to a film thickness of about  $h = 14$ . (ii) We use  $A = 8$  and  $\xi = 2$ . These are typical values found in refs 62 and 63 close to  $T_g$ . (iii) We pose  $\tau_{\text{seg}}^{\text{bulk}} = 1$ .

Observation ii can be quantified by assuming a Cole/Davidson formula<sup>87</sup> for the local dielectric function

$$\varepsilon^*(\omega, y) = \varepsilon_\infty + \frac{\Delta\varepsilon(y)}{[1 + i\omega\tau_{\text{seg}}(y)]^{\gamma(y)}} \quad (52)$$

with

$$\gamma(y) = \begin{cases} \frac{3}{10} + \frac{1}{10}y & 1 \leq y < 4 \\ \gamma_{\text{bulk}} = 0.7 & 4 \leq y < 10 \\ \frac{3}{10} + \frac{1}{10}(15 - y) & 11 \leq y < 14 \end{cases} \quad (53)$$

We use eq 52 because it agrees with the HN function, eq 48, if  $\beta_{\text{HN}} = 1$ , and we found  $\beta_{\text{HN}} \approx 1$  in case study II (Table 1). Equation 53 models the increased stretching on approaching the walls; it mimics the  $y$  dependence reported in Figure 6 of ref 63.

2. We keep the second assumption of case study II but apply eqs 42 and 43 symmetrically to both walls.

3. We keep the third assumption of case study II.

Figure 14 displays the resulting dielectric spectra for setups I and II. We see that the loss spectra of the film are displaced to lower frequencies relative to the bulk (Figure 14a). This reflects the slowing down of the film dynamics encapsulated in eqs 52 and 53. Furthermore, as in case study II, we find that

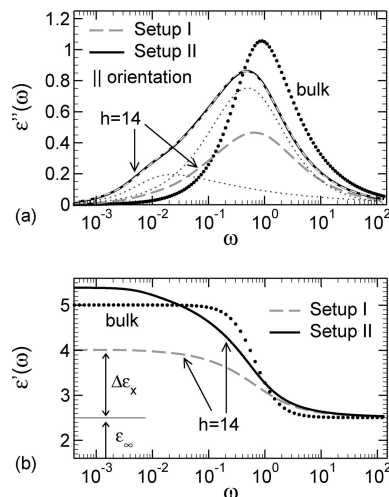


**Figure 14.** (a)  $\varepsilon''(\omega)$  resulting from eq 28 (setup I; gray dashed line) and eq 29 (setup II; black solid line) for a binary Lennard-Jones mixture confined between rough walls<sup>62,63</sup> with film thickness  $h = 14$ . The filled circles represent the bulk results. A fit to eq 54 is indicated by a dashed line which superimposes with the results for setup II. The two separate peaks giving rise to eq 54 are shown by dotted lines ( $j = 1$ : high-frequency HN function;  $j = 2$ : low-frequency HN function). (b) Corresponding  $\varepsilon'(\omega)$ . The value of  $\varepsilon_\infty$  and an example for  $\Delta\varepsilon_x$  ( $x = \text{I, II}$ ),  $\Delta\varepsilon_{\text{I}}$ , is indicated.

**Table 2.** Fit Parameters Obtained from Applying Eq 48 to the Data of Figure 14 (Case Study III)<sup>a</sup>

parameters	setup I	setup II	bulk
$\tau_{\text{HN},1}$	1.4	1.6	1.5
$\gamma_{\text{HN},1}$	1.0	1.2	0.7
$\beta_{\text{HN},1}$	0.74	0.76	1.0
$\Delta\varepsilon_1$	1.3	2.0	2.5
$\tau_{\text{HN},2}$	29	129	
$\gamma_{\text{HN},2}$	0.42	0.26	
$\beta_{\text{HN},2}$	0.85	1.0	
$\Delta\varepsilon_2$	0.2	0.8	
$\omega_{\text{max}}$	0.6	0.5	0.9

<sup>a</sup> These data are derived from simulation results<sup>62,63</sup> for a binary Lennard-Jones mixture between rough, amorphous walls ( $h = 14$ ). The last line gives the values  $\omega_{\text{max}}$  of the peak position of the dielectric loss.  $\omega_{\text{max}}$  and  $\tau_{\text{HN},j}$  are measured in units of  $\tau_{\text{seg}}^{\text{bulk}}$  (see discussion of eq 51 in the text).

the dielectric strength is smaller in setup I than in setup II (Figure 14b). By virtue of eq 40, this finding implies, again as in case study II, that  $\varepsilon''_I(\omega)$  is depressed compared to  $\varepsilon''_{II}(\omega)$ . On the other hand, there are also two features in which the present results differ from those of case study II. First, the peak position of the loss spectrum is closer to the bulk value for setup I than for setup II. Just the opposite was found in case study II. Second, it is not possible to parametrize the dielectric spectra by a single HN function; two HN functions are needed:

$$\varepsilon^*(\omega) = \varepsilon_\infty + \sum_{j=1}^2 \frac{\Delta\varepsilon_j}{[1 + (i\omega\tau_{\text{HN},j})^{\beta_{\text{HN},j}}]^{\gamma_{\text{HN},j}}} \quad (54)$$

The fit parameters are summarized in Table 2. The relaxation time  $\tau_{\text{HN}}$  of the first HN function is close to that of the bulk, whereas  $\tau_{\text{HN}}$  of the second HN function is much smaller. Thus, just on the basis of the data of Figure 14, which represent averages over all layers of the film, one could conclude that there are two distinct processes: a fast one corresponding to a bulklike phase in the film center and a slow one associated with an interfacial region close to the substrate. However, the layer-resolved analysis of  $\phi_q^s(t)$  alluded to above reveals that this interpretation is misleading.<sup>63</sup> The slow process does not result from a distinct interfacial phase, but rather from the smooth gradient<sup>101</sup> in the segmental relaxation which slows down on

approaching the wall. Such an interface-induced gradient in relaxation is consistent with the present results (section 5), other simulation work,<sup>61</sup> and experiments on fluorescent PS<sup>26</sup> and PMMA<sup>96</sup> multilayer films.

## 7. Summary

The present paper consists of two parts: a part dealing with dielectric relaxation in simulations of supercooled polymer films (sections 2.3 to 5) and a part concerned with the numerical calculation of dielectric spectra from the viewpoint that thin films can be modeled as a system of capacitors (section 6).

The first part is inspired by recent work of Barbieri et al.<sup>83</sup> Following this study dipole moments parallel and perpendicular to the chain backbone are introduced into the completed simulation trajectory of our bead-spring model (section 2). This enables us to explore the dielectric response of the segmental and normal modes in time space and, after Fourier transformation, also in frequency space. In the following we summarize the main conclusions from this analysis.

The time correlation function of the total dipole moment of the melt is a collective quantity. For the segmental mode we demonstrate that the collective correlation function agrees with the single-chain correlation function (Figure 2a). Thus, intermolecular correlations between chains can be neglected, an assumption often followed in the literature,<sup>78,81,83</sup> which we prove here for our model.

The segmental dynamics is affected by the interfaces in the film. A layer-resolved analysis (Figures 9 and 10) reveals that segmental dipoles at the free and solid interfaces relax more rapidly than those in the center of the film, which remain bulklike. Because of the faster than bulk relaxation at the supporting wall, we believe that we do not find a confinement induced mode, reported in experiments<sup>54–56</sup> and attributed to strong adsorption of chains in contact with the substrate. A further consequence of the accelerated relaxation induced by both interfaces is that, if we consider bulk and film at the same temperature, the average dynamics of the films is faster than that of the bulk (Figure 6b). This has an impact on the glass transition. The temperature dependence of  $\omega_{\max}$ , where the dielectric loss of the segmental mode peaks, can be well described by a VFT law for film and bulk systems (Figure 6a). The resulting Vogel–Fulcher temperature is lower in the film than in the bulk. Thus, the glass transition temperature of the film is depressed relative to the bulk.

All results summarized in the preceding paragraph are in qualitative agreement with previous work on various mean-square displacements, the incoherent intermediate scattering function, and the shift of  $T_g$  and  $T_c$  with film thickness.<sup>39,40,61</sup>

Further results concern the dependence of the relaxation dynamics on the direction to the plane of the film. We find that the segmental relaxation is isotropic in the film. The relaxation of the normal mode, however, is anisotropic. The perpendicular component of the normal mode  $C_{N,\perp}(t)$  relaxes more rapidly than the parallel component and the relaxation time of  $C_{N,\perp}(t)$  decreases with film thickness. Thus, the total correlation function of the normal mode is dominated by the component parallel to the plane of the film (Figures 7 and 8). Within the range of film thicknesses and chain lengths investigated we find that the relaxation of the parallel component is accelerated relative to the bulk (Figure 7).

The second part of this paper (section 6) differs from the first part: It does not deal with an analysis of simulation results but with an attempt to model dielectric spectra of thin polymer films by a system of capacitors. Certainly, our modeling is tentative and also simplified. For instance, we concentrate on the  $\alpha$ -relaxation, leaving aside other dynamic phenomena, such as the normal mode,<sup>54–56</sup> conductivity contributions,<sup>3,28</sup> or a

confinement-induced mode,<sup>54–56</sup> which are or may be present in experimental spectra. However, our simplified analysis may be justified by the fact that it allows us to elaborate one point: The analysis suggests that the direction of the electric ( $E$ )-field—while unimportant in the bulk—has an impact on the dielectric spectra measured for thin films. In general, the spectra depend on whether the  $E$ -field is perpendicular to the plane of the film (setup I) or parallel to it (setup II). We find that the film spectra—that is, the dielectric response averaged over all layers of the film—do not only depend on the segmental relaxation in each layer but also on the layer-dependent dielectric strength and on  $\epsilon_\infty$ . Dielectric spectra from both setups can thus differ, although the segmental relaxation in each layer of the film is the same for both setups. It might be interesting to see whether these results from our modeling hold up under experimental scrutiny.

**Acknowledgment.** We acknowledge financial support from the European Community's "Marie-Curie Actions" under Contract MRTN-CT-2004-504052 (POLYFILM). J.B. acknowledges financial support by the IUF.

## Appendix. Setup I and II: Real and Imaginary Parts of the Dielectric Function

In section 6.1 we discussed two experimental setups: one where the  $E$ -field is applied perpendicular to the plane of the film (setup I) and the other with the  $E$ -field being parallel to the plane (setup II). These setups lead to different predictions for the average dielectric function  $\epsilon^*(\omega)$  of a film: eq 28 for setup I and eq 29 for setup II. Here we decompose  $\epsilon_i^*(\omega, h)$  and  $\epsilon_{II}^*(\omega)$  into real and imaginary parts and present some results for the case where the dielectric function  $\epsilon_i^*(\omega)$  of layer  $i$  ( $i = 1, \dots, n_l$ ) displays a Debye relaxation.

First, we write

$$\epsilon_i^*(\omega) = \epsilon_i'(\omega) - i\epsilon_i''(\omega) \quad (55)$$

Inserting this equation into eq 28, we obtain for setup I

$$\begin{aligned} \bar{\epsilon}_I'(\omega) &= \frac{\bar{\epsilon}'}{(\bar{\epsilon}')^2 + (\bar{\epsilon}'')^2} \\ \bar{\epsilon}_I''(\omega) &= \frac{\bar{\epsilon}''}{(\bar{\epsilon}')^2 + (\bar{\epsilon}'')^2} \end{aligned} \quad (56)$$

where

$$\begin{aligned} \bar{\epsilon}_I'(\omega) &= \frac{1}{n_l} \sum_{i=1}^{n_l} \frac{\epsilon_i'}{(\epsilon_i')^2 + (\epsilon_i'')^2} \\ \bar{\epsilon}_I''(\omega) &= \frac{1}{n_l} \sum_{i=1}^{n_l} \frac{\epsilon_i''}{(\epsilon_i')^2 + (\epsilon_i'')^2} \end{aligned} \quad (57)$$

Similarly, when inserting eq 55 into eq 29, we obtain for setup II

$$\begin{aligned} \epsilon_{II}'(\omega) &= \frac{1}{n_l} \sum_{i=1}^{n_l} \epsilon_i'(\omega) \\ \epsilon_{II}''(\omega) &= \frac{1}{n_l} \sum_{i=1}^{n_l} \epsilon_i''(\omega) \end{aligned} \quad (58)$$

If we now assume that  $\epsilon_i^*(\omega)$  exhibits a Debye relaxation, i.e.,

$$\begin{aligned} \epsilon_i'(\omega) &= \epsilon_\infty + \frac{\Delta\epsilon_i}{1 + (\omega\tau_i)^2} \\ \epsilon_i''(\omega) &= \frac{\Delta\epsilon_i}{1 + (\omega\tau_i)^2} \omega\tau_i \end{aligned} \quad (59)$$

where  $\Delta\epsilon_i$  and  $\tau_i$  are respectively the dielectric strength and the relaxation time of layer  $i$ , we find for the ratios in eq 57

$$\frac{\varepsilon'_i}{(\varepsilon'_i)^2 + (\varepsilon''_i)^2} = \frac{1}{\varepsilon_\infty + \Delta\varepsilon_i/[1 + (\omega\tau_i)^2]} \times \frac{1}{1 + (\omega\tau_i)^2(1 + \varepsilon_\infty[1 + (\omega\tau_i)^2]/\Delta\varepsilon_i)^{-2}} \quad (60)$$

and

$$\frac{\varepsilon''_i}{(\varepsilon'_i)^2 + (\varepsilon''_i)^2} = \frac{1 + (\omega\tau_i)^2}{(\omega\tau_i)\Delta\varepsilon_i} \frac{1}{1 + (\omega\tau_i)^{-2}(1 + \varepsilon_\infty[1 + (\omega\tau_i)^2]/\Delta\varepsilon_i)^2} \quad (61)$$

When inserting these results into eq 57, we can derive the limiting low-frequency behavior for setup I from eq 56. The result is

$$\varepsilon'_i(\omega \rightarrow 0) = \left[ \frac{1}{n_i} \sum_{i=1}^{n_i} \frac{1}{\varepsilon_\infty + \Delta\varepsilon_i} \right]^{-1} \quad (62)$$

$$\varepsilon''_i(\omega \rightarrow 0) = \left[ \frac{1}{n_i} \sum_{i=1}^{n_i} \frac{1}{\varepsilon_\infty + \Delta\varepsilon_i} \right]^{-2} \left[ \frac{1}{n_i} \sum_{i=1}^{n_i} \frac{\tau_i \Delta\varepsilon_i}{(\varepsilon_\infty + \Delta\varepsilon_i)^2} \right] \omega \quad (63)$$

Similarly, when inserting eq 59 into eq 58, we find for setup II

$$\begin{aligned} \varepsilon'_{II}(\omega \rightarrow 0) &= \varepsilon_\infty + \frac{1}{n_i} \sum_{i=1}^{n_i} \Delta\varepsilon_i \\ \varepsilon''_{II}(\omega \rightarrow 0) &= \left[ \frac{1}{n_i} \sum_{i=1}^{n_i} \Delta\varepsilon_i \right] \omega \end{aligned} \quad (64)$$

For the special choice  $\varepsilon_\infty = 0$  and  $\Delta\varepsilon_i = 1$ , made in case study I, the low-frequency behavior of both setups is given by

$$\varepsilon'_I(\omega \rightarrow 0) = \varepsilon'_{II}(\omega \rightarrow 0) = \omega \langle \tau \rangle \quad (65)$$

where

$$\langle \tau \rangle = \frac{1}{n_i} \sum_{i=1}^{n_i} \tau_i \quad (66)$$

For the choice  $\varepsilon_\infty = 0$  and  $\Delta\varepsilon_i = 1$  we also calculate the full dielectric function because it takes a simple form. From eqs 60 and 61 we obtain

$$\frac{\varepsilon'_i}{(\varepsilon'_i)^2 + (\varepsilon''_i)^2} = 1 \quad \text{and} \quad \frac{\varepsilon''_i}{(\varepsilon'_i)^2 + (\varepsilon''_i)^2} = \omega\tau_i \quad (67)$$

so that we get for setup I

$$\begin{aligned} \varepsilon'_I(\omega) &= \frac{1}{1 + (\omega \langle \tau \rangle)^2} \\ \varepsilon''_I(\omega) &= \frac{\omega \langle \tau \rangle}{1 + (\omega \langle \tau \rangle)^2} \end{aligned} \quad (68)$$

and for setup II

$$\begin{aligned} \varepsilon'_{II}(\omega) &= \frac{1}{n_i} \sum_{i=1}^{n_i} \frac{1}{1 + (\omega\tau_i)^2} \\ \varepsilon''_{II}(\omega) &= \frac{1}{n_i} \sum_{i=1}^{n_i} \frac{\omega\tau_i}{1 + (\omega\tau_i)^2} \end{aligned} \quad (69)$$

## References and Notes

- Donth, E. *The Glass Transition*; Springer: Berlin, 2001.
- Forrest, J. A.; Dalnoki-Veress, K. *Adv. Colloid Interface Sci.* **2001**, *94*, 167.
- Hartmann, L.; Fukao, K.; Kremer, F. In *Broadband Dielectric Spectroscopy*; Kremer, F., Schönhal, A., Eds.; Springer: Berlin, 2003; pp 433–473.
- Kremer, F.; Huwe, A.; Schönhal, A.; Rózański, S. A. In *Broadband Dielectric Spectroscopy*; Kremer, F., Schönhal, A., Eds.; Springer: Berlin, 2003; pp 171–224.
- Roth, C. B.; Dutcher, J. R. In *Soft Materials: Structure and Dynamics*; Dutcher, J. R., Marangoni, A. G., Eds.; Marcel Dekker: New York, 2005; pp 1–38.
- Alcoulabi, M.; McKenna, G. B. *J. Phys.: Condens. Matter* **2005**, *17*, R461.
- Alba-Simionesco, C.; Coasne, B.; Dosseh, G.; Dudziak, G.; Gubbins, K. E.; Radhakrishnan, R.; Sliwinski-Bartkowiak, M. *J. Phys.: Condens. Matter* **2006**, *18*, R15.
- Alba-Simionesco, C.; Dosseh, G.; Dumont, E.; Frick, B.; Geil, B.; Morineau, D.; Teboul, V.; Xia, Y. *Eur. Phys. J. E* **2003**, *12*, 19.
- Srivastava, S.; Basu, J. K. *Phys. Rev. Lett.* **2007**, *98*, 165701.
- Keddie, J. L.; Jones, R. A. L.; Cory, R. A. *Europhys. Lett.* **1994**, *27*, 59.
- Keddie, J. L.; Jones, R. A. L.; Cory, R. A. *Faraday Discuss.* **1994**, *98*, 219.
- Forrest, J. A.; Dalnoki-Veress, K.; Dutcher, J. R. *Phys. Rev. E* **1997**, *56*, 5705.
- Sharp, J. S.; Forrest, J. A. *Phys. Rev. Lett.* **2003**, *91*, 235701.
- Sharp, J. S.; Forrest, J. A. *Phys. Rev. E* **2003**, *67*, 031805.
- Forrest, J. A. *Eur. Phys. J. E* **2002**, *8*, 261.
- Hartmann, L.; Gorbatschow, J.; Hauwede, J.; Kremer, F. *Eur. Phys. J. E* **2002**, *8*, 145.
- Herminghaus, S.; Jacobs, K.; Seemann, R. *Eur. Phys. J. E* **2001**, *5*, 531.
- Herminghaus, S. *Eur. Phys. J. E* **2002**, *8*, 237.
- Herminghaus, S.; Seemann, R.; Landfester, K. *Phys. Rev. Lett.* **2004**, *93*, 017801.
- Grohens, Y.; Hamon, L.; Reiter, G.; Soldara, A.; Holl, Y. *Eur. Phys. J. E* **2002**, *8*, 217.
- Fukao, K.; Miyamoto, Y. *Phys. Rev. E* **2000**, *61*, 1743.
- Fukao, K.; Miyamoto, Y. *Phys. Rev. E* **2001**, *64*, 011803.
- Kim, J. H.; Jang, J.; Zin, W.-C. *Langmuir* **2001**, *17*, 2703.
- Tsui, O. K. C.; Zhang, H. F. *Macromolecules* **2001**, *34*, 9139.
- Fryer, D. S.; Peters, R. D.; Kim, E. J.; Tomaszewski, J. E.; de Pablo, J. J.; Nealey, P. F. *Macromolecules* **2001**, *34*, 5627.
- Ellison, C. J.; Torkelson, J. M. *Nat. Mater.* **2003**, *2*, 695.
- Ellison, C.; Munda, M.; Torkelson, J. *Macromolecules* **2005**, *38*, 1767.
- Priestley, R. D.; Broadbelt, L. J.; Torkelson, J. M.; Fukao, K. *Phys. Rev. E* **2007**, *75*, 061806.
- Lupaşcu, V.; Picken, S. J.; Wübbenhorst, M. *J. Non-Cryst. Solids* **2006**, *352*, 5594.
- Napolitano, S.; Wübbenhorst, M. *J. Phys. Chem. B* **2007**, *111*, 9197.
- Efremov, M. Y.; Olson, E. A.; Zhang, M.; Zhang, Z.; Allen, L. H. *Macromolecules* **2004**, *37*, 4607.
- Huth, H.; Minakov, A. A.; Serghei, A.; Kremer, F.; Schick, C. *Eur. Phys. J. Spec. Top.* **2007**, *141*, 153.
- Fakhraai, Z.; Forrest, J. A. *Phys. Rev. Lett.* **2005**, *95*, 025701.
- A caveat should be mentioned here. While earlier results from dielectric spectroscopy<sup>16</sup> support the finding from ellipsometry studies<sup>14</sup> that the  $T_g$  of i-PMMA films supported on aluminum decreases with film thickness, a recent reanalysis and extension of the data from ref 16 suggests that the reported  $T_g$  shifts are caused by an “erroneous analysis of the experimental results”.<sup>51</sup>
- Fakhraai, Z.; Forrest, J. A. *Science* **2008**, *319*, 600.
- Xu, G.; Mattice, W. L. *J. Chem. Phys.* **2003**, *118*, 5241.
- Torres, J. A.; Nealey, P. F.; de Pablo, J. J. *Phys. Rev. Lett.* **2000**, *85*, 3221.
- Jain, T. S.; de Pablo, J. J. *Phys. Rev. Lett.* **2004**, *92*, 155505.
- Peter, S.; Meyer, H.; Baschnagel, J. *J. Polym. Sci., Part B* **2006**, *44*, 2951.
- Peter, S.; Meyer, H.; Baschnagel, J.; Seemann, R. *J. Phys.: Condens. Matter* **2007**, *19*, 205119.
- Morita, H.; Tanaka, K.; Kajiyama, T.; Nishi, T.; Doi, M. *Macromolecules* **2006**, *39*, 6233.
- Serghei, A.; Huth, H.; Schellenberger, M.; Schick, C.; Kremer, K. *Phys. Rev. E* **2005**, *71*, 061801.
- van Zanten, J. H.; Wallace, W. E.; Wu, W.-I. *Phys. Rev. E* **1996**, *53*, R2053.
- Roth, C. B.; McNerny, K. L.; Jager, W. F.; Torkelson, J. M. *Macromolecules* **2007**, *40*, 2568.
- Napolitano, S.; Lupaşcu, V.; Wübbenhorst, M. *Macromolecules* **2008**, *41*, 1061.
- Dalnoki-Veress, K.; Forrest, J. A.; Murray, C.; Gigault, C.; Dutcher, J. R. *Phys. Rev. E* **2001**, *63*, 031801.
- Roth, C. B.; Dutcher, J. R. *Eur. Phys. J. E* **2003**, *12*, S103.
- Roth, C. B.; Pound, A.; Kamp, S. W.; Murray, C. A.; Dutcher, J. R. *Eur. Phys. J. E* **2006**, *20*, 441.
- O’Connell, P. A.; McKenna, G. B. *Science* **2005**, *307*, 1760.
- Serghei, A.; Tress, M.; Kremer, F. *Macromolecules* **2006**, *39*, 9385.



- (51) Serghei, A.; Hartmann, L.; Kremer, F. *J. Non-Cryst. Solids* **2007**, 353, 4330.
- (52) Jeon, S.; Granick, S. *Macromolecules* **2001**, 34, 8490.
- (53) Kojio, K.; Jeon, S.; Granick, S. *Eur. Phys. J. E* **2001**, 8, 167.
- (54) Kremer, F.; Hartmann, L.; Serghei, A.; Pourcet, P.; Leger, L. *Eur. Phys. J. E* **2003**, 12, 139.
- (55) Serghei, A.; Kremer, F. *Phys. Rev. Lett.* **2003**, 91, 165702.
- (56) Fukao, K. *Eur. Phys. J. E* **2003**, 12, 119.
- (57) Napolitano, S.; Wübbenhorst, M. *Macromolecules* **2006**, 39, 5967.
- (58) Napolitano, S.; Prevosto, D.; Lucchesi, M.; Pingue, P.; D'Acunto, M.; Rolla, P. *Langmuir* **2007**, 23, 2103.
- (59) Napolitano, S.; Wübbenhorst, M. *J. Phys. Chem. B* **2007**, 111, 5775.
- (60) Lund, R.; Willner, L.; Alegria, A.; Colmenero, J.; Richter, D. *Macromolecules* **2008**, 41, 511.
- (61) Baschnagel, J.; Varnik, F. *J. Phys.: Condens. Matter* **2005**, 17, R851.
- (62) Scheidler, P.; Kob, W.; Binder, K. *Europhys. Lett.* **2002**, 59, 701.
- (63) Scheidler, P.; Kob, W.; Binder, K. *J. Phys. Chem. B* **2004**, 108, 6673.
- (64) Böhme, T. R.; de Pablo, J. J. *J. Chem. Phys.* **2002**, 116, 9939.
- (65) Baljon, A. R. C.; Van Weert, M. H. M.; Barber DeGraaff, R.; Khare, R. *Macromolecules* **2005**, 38, 2391.
- (66) Baljon, A. R. C.; Billen, J.; Khare, R. *Phys. Rev. Lett.* **2004**, 93, 255701.
- (67) Kremer, K.; Grest, G. S. *J. Chem. Phys.* **1990**, 92, 5057.
- (68) Pütz, M.; Kremer, K.; Grest, G. S. *Europhys. Lett.* **2000**, 49, 735.
- (69) Soddemann, T.; Dünweg, B.; Kremer, K. *Phys. Rev. E* **2003**, 68, 046702.
- (70) Binder, K.; Horbach, J.; Kob, W.; Paul, W.; Varnik, F. *J. Phys.: Condens. Matter* **2004**, 16, S429.
- (71) Auhl, R.; Everaers, R.; Grest, G. S.; Kremer, K.; Plimpton, S. J. *J. Chem. Phys.* **2003**, 119, 12718.
- (72) Wittmer, J. P.; Beckrich, P.; Meyer, H.; Cavallo, A.; Johner, A.; Baschnagel, J. *Phys. Rev. E* **2007**, 76, 011803.
- (73) Müller, M.; MacDowell, L. G.; Yethiraj, A. *J. Chem. Phys.* **2003**, 118, 2929.
- (74) Serghei, A.; Kremer, F.; Kob, W. *Eur. Phys. J. E* **2003**, 12, 143.
- (75) The reason for why capping polymer films with an aluminum layer appears not to suppress free surface effects is not fully understood. A possible explanation could be that aluminum just coats the polymer surface during the evaporation process, thus preserving the sharp polymer–vacuum interface initially present.<sup>13</sup>
- (76) Schönhals, A. In *Broadband Dielectric Spectroscopy*; Kremer, F., Schönhals, A., Eds.; Springer: Berlin, 2003; pp 225–293.
- (77) Adachi, K.; Kotaka, T. *Macromolecules* **1985**, 18, 466.
- (78) Adachi, K.; Kotaka, T. *Macromolecules* **1988**, 21, 4157.
- (79) Boese, D.; Kremer, F. *Macromolecules* **1990**, 23, 829.
- (80) Petychakis, L.; Floudas, G.; Fleischer, G. *Europhys. Lett.* **1997**, 40, 685.
- (81) Doxastakis, M.; Theodorou, D. N.; Fytas, G.; Kremer, F.; Faller, R.; Müller-Plathe, F.; Hadjichristidis, N. *J. Chem. Phys.* **2003**, 119, 6883.
- (82) Smith, G. D.; Borodin, O.; Paul, W. *J. Chem. Phys.* **2002**, 117, 10350.
- (83) Barbieri, A.; Campani, E.; Capaccioli, S.; Leporini, D. *J. Chem. Phys.* **2004**, 120, 437.
- (84) Chong, S.-H.; Aichele, M.; Meyer, H.; Fuchs, M.; Baschnagel, J. *Phys. Rev. E* **2007**, 76, 051806.
- (85) Meyer, H.; Kreer, T.; Cavallo, A.; Wittmer, J.; Baschnagel, J. *Eur. Phys. J. Spec. Top.* **2006**, 141, 167.
- (86) Hansen, J. P.; McDonald, I. R. *Theory of Simple Liquids*; Academic Press: London, 1986.
- (87) *Broadband Dielectric Spectroscopy*; Kremer, F., Schönhals, A., Eds.; Springer: Berlin, 2003.
- (88) Tuck, A. *Math. Comput.* **1967**, 21, 239.
- (89) Götze, W.; Voigtmann, T. *Phys. Rev. E* **2000**, 61, 4133.
- (90) Angell, C. A.; Ngai, K. L.; McKenna, G. B.; McMillan, P. F.; Martin, S. W. *J. Appl. Phys.* **2000**, 88, 3113.
- (91) The low value of the “strength index”  $D \approx 2.5$  suggests that our polymer model is fairly fragile,<sup>90,102</sup> as typically found for many polymeric glass-formers.<sup>103</sup> However, a caveat should be mentioned here. Our strength index is determined from high- $T$  data where the curvature of the relaxation time in an Arrhenius plot is fairly pronounced. Thus, we may expect  $D$  to change, i.e., to increase, if the simulations could be extended to much lower  $T$ .
- (92) Schüller, J.; Richert, R.; Fischer, E. W. *Phys. Rev. B* **1995**, 52, 15232.
- (93) Forrest, J. A.; Svanberg, C.; Révész, K.; Rodahl, M.; Torell, L. M.; Kasemo, B. *Phys. Rev. E* **1998**, 58, R1226.
- (94) Cavallo, A.; Müller, M.; Wittmer, J. P.; Johner, A.; Binder, K. *J. Phys.: Condens. Matter* **2005**, 17, S1697.
- (95) Starr, F. W.; Schröder, T. B.; Glotzer, S. C. *Macromolecules* **2002**, 35, 4481.
- (96) Priestley, R. D.; Ellison, C. J.; Broadbelt, L. J.; Torkelson, J. M. *Science* **2005**, 309, 456.
- (97) Equivalent circuit models involving systems of capacitors are commonly employed in the interpretation of dielectric properties of inhomogeneous systems having a layered structure with true interfaces (see e.g. Chapter 13 of ref 87 or ref 104). In the context of glass-forming polymer films, the idea of associating layers of the film, which are not separated by true interfaces, with ideal capacitors (i.e., with zero resistances at the electrodes) is presumably correctly attributed to ref 53. The assumption of ideal capacitors is justified because contributions to dielectric spectra from the resistance at the top and bottom electrodes can be removed by a substraction procedure (cf. refs 21 and 28), and there is of course no resistance between the layers inside the film as the layers are not separated by true polymer–electrode interfaces.
- (98) To estimate a typical value for  $\epsilon_\infty$  for our LJ system, we may use the Clausius–Mossotti equation  $(\epsilon_\infty - 1)/(\epsilon_\infty + 2) = (\alpha/\epsilon_0)\rho/3$ , where  $\alpha$  is the polarizability of an LJ monomer and  $\epsilon_0$  is the dielectric permittivity of vacuum. Since the polarization volume  $\alpha/\epsilon_0$  is equal to the monomer volume  $\sigma^3$  ( $= 1$  in our units)<sup>105</sup> and  $\rho \approx 1$  for low  $T$ , we find  $\epsilon_\infty \approx 2.5$ .
- (99) Starr, F. W.; Schröder, T. B.; Glotzer, S. C. *Phys. Rev. E* **2001**, 64, 021802.
- (100) Smith, G. D.; Bedrov, D.; Borodin, O. *Phys. Rev. Lett.* **2003**, 90, 226103.
- (101) The smoothness of this crossover seems hard to reconcile with a layer model, an often invoked interpretation for the relaxation of confined glass-forming liquids (see e.g. refs 58, 59, 106, and 107). This model assumes the coexistence of layers—typically one or two interfacial layers and an inner layer—with distinct mobilities (see e.g. ref 26 for a topical discussion of such models).
- (102) Böhmer, R.; Ngai, K. L.; Angell, C. A.; Plazek, D. J. *J. Chem. Phys.* **1993**, 99, 4201.
- (103) Sokolov, A. P.; Novikov, V. N.; Ding, Y. J. *Phys.: Condens. Matter* **2007**, 19, 205116.
- (104) Svanberg, C. *Macromolecules* **2007**, 40, 312.
- (105) Israelachvili, J. *Intermolecular & Surfaces Forces*; Academic Press: San Diego, 1992.
- (106) Mattson, J.; Forrest, J. A.; Börjesson, L. *Phys. Rev. E* **2000**, 62, 5187.
- (107) Arndt, M.; Stannarius, R.; Gorbatschow, W.; Kremer, F. *Phys. Rev. E* **1996**, 54, 5377.

MA800694V